Li^+ Desolvation in Ether-based Electrolytes Induced by Nitrate Additives Reveals New Insights into High Performance Lithium Batteries

Wandi Wahyudi,† Viko Ladelta,† Leonidas Tsetseris, Merfat M. Alsabban, Xianrong Guo, Emre Yengel, Hendrik Faber, Begimai Adilbekova, Akmaral Seitkhan, Abdul-Hamid Emwas, Mohammed N. Hedhili, Lain-Jong Li, Vincent Tung, Nikos Hadjichristidis, Thomas D. Anthopoulos,* Jun Ming**

W. Wahyudi, Dr. E. Yengel, Dr. H. Faber, B. Adilbekova, A. Seitkhan, Prof. T. D. Anthopoulos
KAUST Solar Center, King Abdullah University of Science and Technology (KAUST), Thuwal 23955-6900, Saudi Arabia.
Email: thomas.anthopoulos@kaust.edu.sa

Prof. J. Ming
State Key Laboratory of Rare Earth Resource Utilization, Changchun Institute of Applied Chemistry, Chinese Academy of Sciences, Changchun 130022, People's Republic of China.
E-mail: jun.ming@ciac.ac.cn

Dr. V. Ladelta, M. M. Alsabban, Prof. L. J. Li, Prof. V. Tung, Prof. N. Hadjichristidis
KAUST Catalysis Center, King Abdullah University of Science and Technology (KAUST), Thuwal 23955-6900, Saudi Arabia.
Email: nikolaos.hadjichristidis@kaust.edu.sa

Prof. L. Tsetseris
Department of Physics, National Technical University of Athens, Athens GR-15780, Greece.

Dr. X. Guo, Dr. A. H. Emwas, Dr. M.N. Hedhili
Core Labs, King Abdullah University of Science and Technology (KAUST), Thuwal 23955-6900, Saudi Arabia.

†These authors contributed equally.

Keywords: electrolyte additives, lithium solvation, graphite anode, lithium batteries, Li-S batteries

Abstract

Electrolyte additives have been widely used to address critical issues in current metal (ion) battery technologies. While their functions as solid electrolyte interface forming agents are reasonably well-understood, their interactions in the liquid electrolyte environment remain rather elusive. This lack of knowledge represents a significant bottleneck that hinders the

development of improved electrolyte systems. Here, the key role of additives in promoting cation (*e.g.*, Li^+) desolvation is unraveled. In particular, nitrate anions (NO_3^-) are found to incorporate into the solvation shells, change the local environment of cations (*e.g.*, Li^+) as well as their coordination in the electrolytes. The combination of these effects leads to effective Li^+ desolvation and enhanced battery performances. Remarkably, the inexpensive $NaNO_3$ can successfully substitute the widely used $LiNO_3$ offering superior long-term stability of Li^+ (de-)intercalation at the graphite anode and suppressed polysulfide shuttle effect at the sulfur cathode, while enhancing the performance of Li-S full batteries (initial capacity of 1153 mAh g^{-1} at 0.25C) with Coulombic efficiency of ≈100% over 300 cycles. This work provides important new insights into the unexplored effects of additives and paves the way to developing improved electrolytes for electrochemical energy storage applications.

1. Introduction

The continuously increasing demand for high-density energy storage devices such as high voltage Li-ion, Li-S, and Li-O_2 batteries has raised a new challenge of developing electrolytes beyond the conventional ethylene carbonate-based solutions.[1] To date, several critical issues associated with electrolyte solutions remain outstanding and include: (i) surficial corrosion of the cathode in Li-ion batteries (*e.g.*, $LiMO_2$, M=Ni/Co/Mn);[2] (ii) graphite exfoliation due to Li^+-solvent co-insertion (*e.g.*, in propylene carbonate and most ether-based electrolytes);[3] (iii) polysulfide shuttle effect in Li-S batteries;[4] and (iv) side-reaction of electrolytes in Li-O_2 batteries.[5] To address some of these issues, researchers have introduced super-concentrated electrolytes (3.6 - 27.8 Molar, M) as a means to mitigate severe electrolyte decomposition and stabilize the electrodes (*e.g.*, lithium metal and graphite anodes),[3b, 6] which have also enabled the use of previously unexplored solvents as electrolytes, including water,[7] dimethyl sulfoxide,[8] and acetonitrile.[9] However, this pragmatic approach is dilemmatic as it increases the cell cost, the super-viscous solution suppresses ionic conductivity (<1.0 mS cm^{-1} at room

temperature), practically difficult to control the electrolyte quantity upon mass production of batteries, and hard to achieve a relatively good wettability compared to the dilute electrolytes.[6c, 10] In the case of Li-S batteries, the slow ion transport in the highly viscous solutions causes additional issues such as slow polysulfide conversion kinetics and accumulation of polysulfide on the separator.[11] An alternative but highly promising strategy relies on the introduction of suitable additives to the electrolytes.[12] Despite the encouraging results, however, detailed understanding of the function of additives on the electrolyte structure and their interactions with the solvents remains elusive.

Electrolyte additives have been shown to positively affect the performance of Li-ion batteries via the formation of an efficient solid electrolyte interphase (SEI) layer that stabilizes the electrodes.[13] This is similar to commonly used additives in the field of Li-S batteries, such as RNO_3 (R = Li, Na, K, La, and Cs),[14] P_2S_5,[15] and LiI[12b], which have been shown to alleviate the polysulfide shuttle effect through passivation of the lithium anode surface by the SEI layer. Although the SEI theory has become popular over the past two decades, detailed knowledge concerning the exact function of additives in the Li^+ solvation structure of electrolytes remains insufficient.

Herein, we report on the critical role of additives in suppressing Li^+ solvation in electrolytes that extends beyond their known SEI function. Taking ether-based electrolytes as prototypical examples using 1,3-dioxolane (DOL) and 1,2-dimethoxyethane (DME) solvents, we show that Li^+ solvation is dependent on the presence of additives and responsible for the electrochemical reactions at the electrodes. Additives, such as nitrates (*i.e.*, $LiNO_3$ and $NaNO_3$), are found to interact with the Li^+ solvation shells and change the local environment of the Li^+ ions as well as Li^+ coordination, resulting in improved Li^+ desolvation and enhanced battery performances. In particular, the Li^+ desolvation is shown to be responsible for the efficient Li^+ intercalation at the graphite anode as well as for the suppression of the polysulfide shuttle effect at the sulfur cathode. Additionally, properties of the SEI formed on the graphite electrodes were

studied *in-situ* using temperature-variable X-ray diffraction (T-XRD) measurements, providing unique insights into the stability of graphite electrodes promoted by the electrolyte. By exploiting the beneficial effects of Li^+ desolvation, we demonstrate, for the first time, superior cycle performance of Li^+ (de-)intercalation at graphite using an ether-based electrolyte over 250 cycles (340 mAh g^{-1}, 91.4% theoretical capacity of graphite) using $NaNO_3$ as an inexpensive alternative additive. The Li-S full battery, comprising a graphite anode and a sulfur cathode, exhibits improved long-term stability (initial capacity of 1153 mAh g^{-1}) with Coulombic efficiency of nearly 100% at 0.25C over 300 cycles. The present work not only provides important new insights into the elusive role of additives on the functioning of battery electrolytes, but also demonstrates a safer Li-S full battery technology with remarkably enhanced performance as compared to the current state-of-the-art.[3a, 3b, 8, 16]

2. Results and Discussions

2.1. Effects of Additives on Li^+ Desolvation in the Electrolytes

The effect of additives on the physicochemical properties of electrolytes, in terms of viscosity and Li^+ transference number (t_{Li+}), is presented in **Figure 1a-b**. We compare several salient features of the studied electrolytes, from dilute to highly concentrated systems: i) The electrolytes used in this work are more dilute (lowest viscosity in the range of 2.8 - 6.5.6 cP as compared to the highly concentrated electrolytes with viscosity 72 - 239 cP, **Table S1**) due to the lower concentration of Li salt and as such favors rapid ion transport.[6b, 6c] We find that viscosity of the electrolyte changes only slightly upon the addition of the additives, highlighting the possibility of tuning the electrolyte's properties while still maintaining a low viscosity. ii) The Li^+ transference number (t_{Li+}) in the electrolytes is also tunable by the additives, which is indicative of the influence of the latter on the coordination of Li^+ in the solvation structures *i.e.*, Li^+-$TFSI^-$ ion pairs or Li^+-solvent clusters. Considering the recent strategy of super-

concentrated electrolytes to obtain successful battery reactions at graphite and lithium electrodes in non-carbonate electrolytes (**Figure 1a**) such as 7.0 M LiTFSI in DOL-DME[6c] and 21.0 - 27.8 M LiTFSI in H_2O,[7a, 17] our strategy offers important economic advantages as it relies on lower salt concentration (*e.g.*, 2.5 M LiTFSI) and inexpensive additives.

The Li^+ transference number of electrolytes with $LiNO_3$ or $NaNO_3$ (t_{Li+} = 0.55 and t_{Li+} = 0.50, respectively) decreases as compared to the pristine system (t_{Li+} = 0.68) in **Table S1**. On the contrary, addition of Li_2SO_4 or Li_3PO_4 leads to higher t_{Li+} (t_{Li+} Li_2SO_4 = 0.77; t_{Li+} Li_3PO_4 = 0.79). The latter observation might be the result of different coordination of anions in the electrolyte, as will be discussed later. To this end we note that the use of additives alters t_{Li+} by up to 35% with respect to the pristine one, which is comparable to the concentrated electrolytes in carbonate and ether solvents.[6-7, 9, 16b, 18] Moreover, additives such as LiBr are also known to raise t_{Li+} to imaginary values in excess of 1.0 due to interference from the oxidation reaction along the polarization (**Figure S1**).[18b] Overall, our results suggest that the additives can potentially change the Li^+ solvation structure in the electrolyte solutions.

The effects of additives on the local environment of Li^+ ions in the electrolytes were studied using nuclear magnetic resonance (NMR) spectroscopy. The ^7Li NMR spectra of the electrolytes (**Figure 1c**) show that additives lead to a very different environment for the Li^+ ions. Down-field displacement of the NMR spectra towards more positive chemical shift values indicates that the Li^+ nuclei are deshielded by the surrounding electron cloud, whereas the up-field displacement indicates an opposite trend. The addition of Li_2SO_4 and Li_3PO_4 results in more shielded Li^+ ions than that in the pristine electrolyte (-1.1048 ppm) towards more negative chemical shifts of -1.1070 ppm and -1.1126 ppm, indicating stronger Li^+ solvation. In contrast, other additives such as $NaNO_3$, $LiNO_3$, LiCl, LiBr, LiI, and $LiClO_4$ lead to deshielded Li^+ ions by showing more positive ^7Li chemical shifts than that of the pristine electrolyte, which indicate an effective Li^+ desolvation. Thus, and for the purpose of this study, we focused on Li_2SO_4,

Li_3PO_4, $NaNO_3$, $LiNO_3$, and LiBr additives as they induce a wide effect on Li^+ solvation and desolvation with respect to the pristine electrolyte.

We further studied the effects of additives on the Li^+ solvation structure by Raman spectroscopy. The S-N stretching band of $TFSI^-$ at 730 - 760 cm^{-1} (**Figure 1d**; **Figure S2**)[3a, 19] is much broader in the electrolyte than that in the LiTFSI salt, indicating variations of Li^+-$TFSI^-$ coordination in the electrolytes that are also affected differently by additives. Inserting Li_2SO_4 and Li_3PO_4 into the electrolytes results in the S-N band shift towards a free stretching vibration (lower wavenumber), which implies that Li^+ coordination with $TFSI^-$ is hampered and the population of $TFSI^-$ free ions increases.[3a, 9] Thus, migration of the Li^+-solvent clusters is more dominant than Li^+-$TFSI^-$ ion pair in the electrolytes, which are then responsible for the increased Li^+ transference number. By contrast, the S-N band slightly shifts to a higher wavenumber in the electrolyte solution with LiBr and then shifts further to the higher wavenumber with the addition of $LiNO_3$ and $NaNO_3$, indicating a significant increase in Li^+-$TFSI^-$ coordination and a decrease in $TFSI^-$ free ion population. As a result, the t_{Li+} decreases in electrolytes incorporating $LiNO_3$ or $NaNO_3$ due to the slower migration of Li^+-$TFSI^-$ pair compared to the Li^+-solvent cluster. The C-O stretching modes of DME (800 - 880 cm^{-1}) shifts more than that of DOL (920 - 950 cm^{-1}) in the electrolytes,[6b, 20] indicating that Li^+ solvation by DME is significantly stronger than by DOL, and the peak shift is also affected by additives. Deconvolution of the $TFSI^-$ S-N band (**Figure 1e**) confirms that electrolyte solutions with Li_2SO_4 and Li_3PO_4 consist primarily of $TFSI^-$ free ions (737 cm^{-1}) - FI, $TFSI^-$ does not interact with Li^+. In contrast, the presence of nitrate additives increases the population of Li^+-$TFSI^-$ ion pairs, *i.e.*, loose ion pairs at 741 cm^{-1} (LIP, a $TFSI^-$ indirectly interacts with Li^+) and intimate ion pairs at 745 cm^{-1} (IIP, a $TFSI^-$ interacts with one Li^+).[19] Notably, both nitrate additives ($LiNO_3$ and $NaNO_3$) not only suppress the population of $TFSI^-$ free ions to below 10% (**Figure 1f**), but also indicate the presence of aggregate ion pairs at 747 cm^{-1} (AIP, a $TFSI^-$ interacts with ≥2 Li^+). The aggregate ion pairs have been previously reported to be unique Li^+ coordination

that appears in high concentration electrolytes and are beneficial for Li^+ transport,[6b, 9, 18a] but we show that the pairs also can appear in the dilute electrolytes by adding nitrate additives.

In order to elucidate key atomic-scale details of the pertinent molecular complexes, we performed Density Functional Theory (DFT) calculations. **Figure S3** shows the structures of a number of LiTFSI-related complexes in the gas phase, along with the calculated vibrational frequencies of their S-N stretching modes (displacements are depicted with green arrows). Based on these results, the addition of a Li^+ cation to a $TFSI^-$ anion shifts the S-N stretching mode by 1.8 cm^{-1}, and then the addition of a NO_3^- anion or a $LiNO_3$ molecule causes an extra shift by 2.9 cm^{-1} or 3.4 cm^{-1}, respectively. These shifts are in good agreement with the analysis of **Figure 1d**, supporting the distinction of $TFSI^-$-related species to free, loose, intimate, and aggregate ion pairs.

With respect to Li^+ coordination, DFT results find that in a DOL-only environment, a Li^+ cation is trapped by four molecules in an almost tetrahedral geometry (**Figure 1g**). In the case of a DME-only solvent, the Li^+ cation is six-fold coordinated to the O atoms of three DME molecules (**Figure 1h**). When a $TFSI^-$ anion is added, it takes the place of, respectively, a DOL or a DME molecule in a five-fold or six-fold coordination. The original solvation shell is modified further when a NO_3^- anion that is brought to its neighborhood replaces one or two of the nearest DOL or DME molecules, as shown for example in **Figure 1i**. The full details of the dynamics of such complexes are beyond the scope of a DFT study. Nevertheless, we should note that the above-mentioned changes in the coordination of the Li^+ cation are consistent with the proposed desolvation hypothesis. By the same token, the relatively small size of the NO_3^- anion and its binding to the Li^+ cation might play a role in enhancing the diffusivity of the latter. Our findings confirm that incorporation of additives, particularly the nitrates $LiNO_3$ and $NaNO_3$, affects the Li^+ solvation behavior by mediating the desolvation of Li^+ from the solvated structure more efficiently than the super-concentrated electrolyte strategy.

2.2. Li^+ Desolvation Mechanism by Nitrate Additives

The Li^+ desolvation mechanism was further studied by increasing the concentration of the nitrate additive, 0.1 M, 0.2 M, 0.3 M, and 0.4 M of $NaNO_3$. Raman spectra of the electrolytes show a gradual shift in the S-N stretching band of $TFSI^-$ towards higher wavenumber upon the addition of $NaNO_3$ (**Figure S4**), which indicates that NO_3^- anions improve the Li^+ coordination with $TFSI^-$ anions. The effect of nitrate anions on the Li^+ desolvation is further corroborated by NMR spectroscopy. **Figure 2**a shows that ^7Li NMR spectra of the pristine electrolyte gradually shift to more positive chemical shift values of -1.0444 ppm, -0.9883 ppm, -0.9374 ppm, and -0.8875 ppm with the addition of 0.1 - 0.4 M $NaNO_3$. As oxygen in the anions ($TFSI^-$ and NO_3^-) are less electronegative than that in the DOL and DME molecules, deshielded ^7Li NMR spectra of the electrolytes upon the addition of nitrate additive suggests the progressive Li^+ desolvation from the DOL-DME solvents and improved Li^+ coordination with oxygen in the anions.[21] In addition, dynamic light scattering (DLS) spectra of the electrolytes (**Figure 2b**) show that the size of solvation clusters increases with increasing concentration of the nitrate additive, *i.e.*, 944.5 nm (without additive), 987.2 nm (0.1 M), 1109.3 nm (0.2 M), 1592.8 nm (0.3 M), and 2342.9 nm (0.4 M). The latter suggests that NO_3^- anions are incorporated into the solvation shells and promote Li^+ desolvation.

Direct evidence of the relation between Li^+ desolvation and battery performances is provided by the gradual Li^+ desolvation upon the increase of $NaNO_3$ concentration, which is accompanied by a progressive improvement of the reversible Li^+ (de-)intercalation at the graphite electrode (**Figure 2c**). Upon discharging to 0.01 V, the pristine electrolyte indicates a severe electrolyte decomposition at around 1.0 to 0.5 V and typical Li^+-solvent co-insertion at the potential of around 0.3 V. The electrolyte decomposition and Li^+-solvent co-insertion are progressively suppressed with the addition of $NaNO_3$ from 0.1 to 0.4 M concentration until we obtain the typical Li^+ intercalation plateau at the potential of below 0.25 V. Upon charging to 3.0 V we expect backward reactions of Li^+ de-intercalation from graphite and then Li platting

on the lithium metal anode. The pristine electrolyte retains a low charging capacity of 114 mAh g^{-1}, indicating a poor Li^+ de-intercalation in the graphite because of the severe Li^+ solvation and Li^+-solvent co-insertion. The Li^+ de-intercalation process improves significantly upon the addition of the nitrate additive, such as that seen in cells with 0.4 M $NaNO_3$-added electrolyte, which achieves a charging capacity of 361 mAh g^{-1} (Figure 2c). To this end we note that both Li^+ intercalation and de-intercalation processes during discharging and charging of the cells are strongly affected by the $NaNO_3$ additive, as is the battery performance further highlighting its relation with the Li^+ desolvation process induced by the additive.

To further study the effect of nitrate additives on the Li^+ desolvation mechanism, we measured the ^1H NMR spectra of electrolytes (**Figure 2d**). When using DOL as a single solvent, all ^1H spectra features associated with DOL are found to shift up-field to a lower chemical shift (**Figure 2d**, red curve), with the LiTFSI salt quickly dissociating in the DOL and forming a transparent solution (**Figure 2e** left). The latter observation indicates that all oxygen atoms in the solvent molecules interact with Li^+ cations. Once the electron cloud in the DOL is polarized to O atoms, the ^1H of CH_2-O is de-shielded and the chemical shift is expected to shift down-field to a higher chemical shift. Interestingly, we observe a non-trivial behavior in the electrolyte since N^- in the $TFSI^-$ anion is an electron-cloud-rich atom; thus it shields the electron-deficient CH_2 in the solvent. The latter assumption is confirmed by the appearance of a new peak in the DOL + LiTFSI solution at 4.51 ppm (**Figure 2d**, right inset, and illustration in **Figure 2e** left). Additionally, **Figure 2d** (right inset, blue curve) shows that $NaNO_3$ in the DOL + LiTFSI solution results in a new chemical peak shift up-field to 4.45 ppm, which indicates that the acidic ^1H in the solvating DOL also interacts with NO_3^-. The reason for the greater up-field shift is the additional shielding effect of the NO_3^- anion as NO_3^- is also an electron-rich species that donates negative charge to the electron-deficient CH_2 group in DOL (**Figure 2e** right), which then may weaken the Li^+ solvation by the solvent molecules.

Dissolving LiTFSI in DME at room temperature results in the formation of a gel-like solution (**Figure 2f** left), which could be due to the formation of extended solvation clusters. We thus collected the NMR spectra of this solution under mild heating at 40 °C in order to convert the gel-like solution into its liquid state. A clear displacement of ^{1}H spectra in the DME + LiTFSI solution is observed clearly highlighting the effect of temperature (**Figure 2d**, orange curve). The solution returns back to its gel-like form upon cooling to room temperature, suggesting an unfavorable phase transformation of the DME + LiTFSI solution for battery electrolytes. Interestingly, adding $NaNO_3$ to the solution at room temperature leads to fast dissociation of the gel-like structure into a dilute and transparent solution (**Figure 2f** right). Additionally, the DME + LiTFSI solution shows evidence of interactions between the electron-deficient ^{1}H in DME molecules and N^{-} in the $TFSI^{-}$ anions, as a new peak appears at 4.34 ppm followed by a shift further up-field to 4.27 ppm upon addition of $NaNO_3$ (**Figure 2d** right inset, purple curve). The latter observation is indicative of coordination between electron-deficient ^{1}H in the solvent and NO_3^{-} from the additive in the same manner as the solutions with DOL, which helps the Li^{+} desolvation. Moreover, **Figure 2d** (left inset) shows that Li^{+} coordination with DME is much stronger than with DOL molecules as the ^{1}H peaks of the solvating DME shift further up-field (0.22 ppm) than that of the solvating DOL (0.08 ppm), in good agreement with the Raman data (**Figure 1d**).

The mechanistic insight on the coordination between the NO_3^{-} and ^{1}H of the solvent molecules was further corroborated by electron paramagnetic resonance (EPR, **Figure 2g**) measurements. A strong unpaired electron signal centered at value g=1.872 appears, indicating a strong interaction between the electron-deficient ^{1}H in the solvents and the NO_3^{-} anion, with a strong shielding effect. These results confirm that the additives bearing strong electronegative anions, such as nitrate, can effectively enhance Li^{+} desolvation in the electrolyte.

2.3. Assessing Roles of SEI and Li^+ Desolvation

Next we considered the role of Li^+ desolvation over the SEI formation on the graphite electrode. Formation of the SEI in this particular battery system appears at ~1.7 V during discharge and cyclic voltammetry of Li-graphite half-cells (**Figure S5b-c**; **Figure S6**a). Analysis of the surface morphology of the graphite electrode cycled with nitrate additives using a scanning electron microscope (SEM), shows a smooth surface of SEI (**Figure S7**), whereas those cycled without the additive or using other types of additives, exhibit rough surfaces of SEI which is indicative of severe electrolyte decomposition. X-ray photoelectron spectroscopy (XPS) measurements of the C 1s, O 1s, F 1s, and Li 1s spectra (**Figure S8**) show that the SEI layers formed from electrolytes with and without nitrate additive, consist of typical organic and inorganic compounds of previously reported CH_2OCO_2Li, $ROCO_2Li$, and LiF.[22] However, the SEI formed from the electrolyte containing the nitrate-additive contains less oxygen, fluorine, and sulfur elements that are associated with LiTFSI (**Table S2**). Both morphology and elemental analysis on the SEI indicate that nitrate anions improve the stability of electrolytes against a severe decomposition during battery operation.

We further analyzed the SEI using *in-situ* temperature-variable X-ray diffraction (T-XRD), differential scanning calorimetry (DSC), and thermal gravimetric (TG) measurements to understand the thermal behavior of the SEI on graphite. All samples were washed with DOL-DME and dried in vacuum at room temperature prior to the analysis in order to remove chemical residues such as remaining electrolyte. The graphite cycled with the nitrate-added electrolyte shows a consistent graphitic peak at $2\theta \approx 26.5°$ up to 400 °C (**Figure 3a**). The peak is not observed in graphite cycled in the pristine electrolyte (inset **Figure 3a**), but it appears (with much lower intensity) after annealing at 225 °C with no significant change in the morphology of SEI before and after the measurement (**Figure 3b**). DSC analysis shows two exothermic peaks at 225 °C and 325 °C from the graphite cycled in the pristine electrolyte (**Figure 3c**). Both features are associated with the removal of co-inserted Li^+-solvent complexes[23]

accompanied by a weight loss of 17.8% as seen in the TG measurements. Notably, the graphite electrode cycled using nitrate-added electrolyte appears to be free from co-inserted Li^+-solvent complexes since the DSC measurements show no exothermic peak in the range 225 - 325 °C while the weight loss is very small and around 4.5%. From these results, we conclude that the two primary processes responsible for the failure of graphite electrode are, (i) the formation of a thick SEI layer due to severe electrolyte decomposition, and (ii) Li^+-solvent co-insertion due to the strong Li^+ solvation effect.

In view of these findings, we decided to revisit the SEI theory in order to gain an improved understanding of the processes that affect battery performance the most. For the purpose of this experiment, the cells were firstly charged-discharged for three cycles, and then disassembled inside an argon-filled glovebox. The graphite electrodes were then washed and dried under vacuum at room temperature, and new cells with different electrolytes were incorporated for further cycling (**Table S3)**. The obtained results shown in **Figure 3d** and **Figure S9a** indicate that both $LiNO_3$ and $NaNO_3$ are interchangeable without impairing the reversibility of Li^+ intercalation, as they show similar characteristics of voltage profiles before and after electrolyte exchange. Notably, the discharge curve of the second cell with $LiNO_3$ indicates no further formation of the SEI on the graphite after the additives are exchanged. In contrast, the Li^+ intercalation becomes irreversible when the electrolyte contains LiBr or Li_2SO_4 due to the Li^+-solvent co-insertion. Moreover, in graphite electrodes that were initially cycled in the latter electrolyte-additive systems (**Figure 3e** and **Figure S9b**), Li^+-solvent co-insertion appears to dominate, causing graphite exfoliation. To this end, we observe no Li^+ intercalation even when electrolytes are replaced with those containing the nitrate additives (*i.e.*, $LiNO_3$ and $NaNO_3$). These experimental results provide direct evidence that the SEI is not the only element determining the reversibility of the reactions at the graphite electrode and Li^+ desolvation in the electrolyte, which is affected by the nitrate additive, plays an equally important role.

The schematics in **Figure 3f-g** depict the proposed function of Li^+ desolvation at the electrolyte-electrode interface along with the presence of SEI layer. The effective Li^+ desolvation induced by the nitrate anions enables a successful Li^+ ion transfer from the solvation complexes via the SEI towards the structure of graphite electrode at the typical potential of below 0.25 V, which results in the reversible Li^+ intercalation and well-preserved graphite structure (**Figure 3f**; Eq. 1):

Li^+ intercalation: Li^+-solvent + $C_6 \rightleftarrows LiC_6$ + solvent (1)

Li^+-solvent co-insertion: Li^+-solvent + $C_6 \rightarrow C_6/Li^+$-solvent + decomposition (2)

In the absence of nitrate anions, Li^+ ions cannot release from the solvated complex in the electrolyte since the Li^+-solvent interactions are strong. As a result, and despite the presence of the SEI layer on the graphite electrode, the Li^+-solvent complexes can still penetrate through the SEI layer and co-insert into graphite (**Figure 3g**; Eq. 2). The result of Li^+-solvent co-insertion upon repeated charge-discharge cycles of the cells is the continuous electrolyte decomposition and graphite exfoliation, which is evident in **Figure S10**.

2.4. Benefits Associated with Li^+ Desolvation

In addition to the evidence for Li^+ desolvation by additives, we studied the degree of desolvation and its benefits in Li-graphite half-cells, where we observe clear Li^+ intercalation and Li^+-solvent co-insertion mechanisms (**Figure 4a**). We observe the co-insertion of Li^+-solvent into graphite at potential of below 3.0 V[24] upon discharging the cells without any additive, as well as with Li_2SO_4, Li_3PO_4, LiF, LiCl, LiBr, LiI, and $LiClO_4$ present. The Li^+-solvent co-insertion is irreversible upon recharging and leads to a poor life cycle of the cells, as confirmed by cyclic

voltammogram analysis that shows several reduction peaks but no backward oxidation reaction (**Figure S6a**). The poor Li^+ desolvation by the additives and the inferior graphite performance (due to Li^+-solvent co-insertion) are consistent with the Raman and NMR analysis in **Figure 1**. Additionally, Br^- and I^- anions show side reactions causing the electrolytes to become unstable during charging beyond 2.4 V, and causing Cu dissolution due to the continuous oxidation of the copper current collector (**Figure S6a**; **Figure S7h**; inset **Figure 4a**). Importantly, we observe a reversible Li^+ (de-)intercalation at graphite[24a, 25] with a very stable cycle performance in the nitrate-added ($LiNO_3$ or $NaNO_3$) electrolytes (**Figure 4b**). The absence of the Cu element on the graphite after a long-term cycle demonstrates good chemical stability of the electrolyte with respect to the copper current collector (inset in **Figure 4b**), while the good crystallinity of the cycled graphite electrode implies the excellent capability of the nitrate additives ($LiNO_3$ and $NaNO_3$) to suppress the Li^+-solvent co-insertion into graphite (**Figure S10**). **Figure 4c-d** show that cells with $LiNO_3$ and $NaNO_3$ exhibit a highly stable capacity retention of 340 mAh g^{-1} over 100 cycles with Coulombic efficiency of nearly 100%. Cells utilizing other additives (**Figure 4c** and **Figure S5j**) show a significantly lower capacity retention with clearly visible decay; the capacity retention after 100 cycles is 20.8% (Li_2SO_4) and 27.6% (Li_3PO_4) of the theoretical capacity of graphite (372 mAh g^{-1}), respectively. To demonstrate the superior stability that the $NaNO_3$ additive offers, we extended the cycle performance of the cell to 250 cycles. Evidently, the cell exhibits an excellent stability with a capacity retention of 91.4% and negligible capacity decay. To our knowledge, the demonstrated stability of Li^+ (de-)intercalation for graphite in the ether-based electrolytes is among the highest stability reported to date.[3a, 3b, 8, 16b]

Next we investigated the effects of Na^+ ions in the electrolyte on the Li^+ intercalation into graphite at a high current density rate. **Figure 4e** shows that the discharge capacity of the cell with $LiNO_3$-added electrolyte at dynamic C-rate of 0.05C, 0.1C, 0.5C, 1C, 3C, and 5C is 341, 332, 317, 273, 120, and 28 mAh g^{-1}, while the cell with $NaNO_3$-added electrolyte shows a comparable discharge capacity of 345, 337, 313, 264, 113, and 23 mAh g^{-1}, respectively.

Remarkably, both cells retain their initial capacity at 0.5C after cycling at 5C, suggesting good reversibility of Li^+ (de-)intercalation into graphite even at a high current density rate. Furthermore, **Figure 4f** shows identical charge-discharge curves of the cells with $LiNO_3$ and $NaNO_3$ additives during the C-rate performance, indicating that the presence of Na^+ ions in our electrolyte does not impede the battery performance. Our observation is reasonable because the concentration of Na^+ ions is very small compared to that of Li^+ in the 0.4 M $NaNO_3$ + 2.5 M LiTFSI electrolyte, *i.e.*, 3.2×10^{-5} mole mL^{-1} and 250×10^{-5} mole mL^{-1} for Na^+ and Li^+. Moreover, the fact that Na^+ ion is much heavier and larger than Li^+ ion leads to the sluggish kinetics of Na^+ intercalation,[26] which has been known as a great challenge in developing sodium-ion batteries (NIBs). Our XPS analysis confirms that the atomic concentration of Na in the SEI formed from $NaNO_3$-containing electrolyte is only 0.03% (Figure S8 and Table S2), which is a negligible amount. However, we have found that the use of $NaNO_3$ additive in the lithium battery systems is useful as Na^+ ions do not affect the battery performance even at high C-rate, neither the microstructure of SEI.

2.6. Implications in Performance and Safety of Li-S Battery

We have also investigated the relation between Li^+ desolvation and the performance of sulfur cathodes in the Li-S batteries. We find that tuning the electrolyte structure using additives is by far a simpler and more efficient strategy than the use of highly concentrated electrolytes.[3b, 6c, 27] By employing 0.1 - 0.4 M concentration of $NaNO_3$ additives in the electrolytes, we show that the progressive Li^+ desolvation (**Figure 2a**; **Figure S4**) is accompanied by improvement in the Li-S battery performance. **Figure 5a** shows that the Li-S cell without nitrate additive shows the capacity of 231.5 mAh g^{-1} in the first plateau (Q1) and 212.8 mAh g^{-1} in the second plateau (Q2). The obtained capacity gradually increases with the addition of nitrate additive, which raises up to 409.3 mAh g^{-1} in the first plateau (Q1) and 324.3 mAh g^{-1} in the second plateau

(Q2) for 0.4 M $NaNO_3$. We also observe that the progressive Li^+ desolvation, induced by the presence of the nitrate additive, is followed by a gradual improvement in the Coulombic efficiency (CE) over long-term cycles of the Li-S cells (**Figure 5b**). The improvement in performance becomes clear after a few cycles, which continue to improve and stabilizes over 100 cycles. The cell without additive shows low and deteriorating CE upon long-term cycling, whereas those with $NaNO_3$ show higher and more stable CE of near 100%. We also see the CE to gradually increase during the first 15 cycles upon $NaNO_3$ addition (0.1 - 0.4 M), which indicates that the nitrate anions help to suppress the polysulfide dissolution into the electrolytes.

It has been previously reported that the suppression of the polysulfide shuttle effect is not only influenced by the solubility of polysulfide in the electrolyte, but also by the passivation of the lithium metal anode[14a, 24b] and the physical entrapment of soluble polysulfide by separator/cathode microstructure.[1a, 11b, 12b] **Figure 5c** and **Figure S11a-c** show that in the case of a Li-S battery equipped with a pre-coated glass fiber separator, the $LiNO_3$-added electrolyte improves the Li-S cell by enhancing the CE (nearly 100%) over long-term cycles at 0.25C, which is indicative of improved sulfur utilization and suppressed polysulfide shuttle effect. **Figure 5d** and **Figure S11d** show that $NaNO_3$ yields similar cell performance as $LiNO_3$, further supporting its tremendous potential as an alternative to $LiNO_3$ due to its lower cost. This re-confirms the similar effect of $LiNO_3$ and $NaNO_3$ on Li^+ desolvation from the solvation structure, which then suppresses the shuttling polysulfide. By contrast, electrolytes incorporating the other additives, show low capacity retention and Coulombic efficiency, which can be assigned to the poor Li^+ desolvation that leads to the polysulfide shuttle effect (**Figure S6b**). This is an important finding as it highlights a new approach of minimizing the polysulfide shuttle effect in Li-S batteries by suppressing Li^+ solvation. Most importantly, our additive-based approach differs from the general interpretation and commonly used strategy of forming an SEI layer on the metallic lithium anode. We observe that the absence of additive can lead to a difficult Li^+ desolvation from the solvation structure which then hampers sulfur/polysulfide conversion

reactions (equation 3), resulting in polysulfide shuttle effect and low utilization of sulfur. In contrast, $LiNO_3$ and $NaNO_3$ can improve the Li^+ desolvation, which then enables the effective polysulfide reactions with Li^+ and hence helping to suppress the polysulfide shuttle effect.

$$S_8 + 2Li^+ + 2e^- \rightleftarrows Li_2S_x + Li^+ + e^- \rightleftarrows Li_2S;\ (4 \leq x \leq 8) \quad (3)$$

Finally, we studied the electrochemical performance of complete Li-S full batteries with a lithiated graphite anode in an effort to address the safety issues associated with the use of highly reactive lithium metal anodes (**Figure 5e**). Cells based on the $NaNO_3$-added electrolyte exhibit an initial capacity of 1153 mAh g^{-1} and Coulombic efficiency of nearly 100% over 300 cycles at 0.25C (**Figure 5f-g**). To our knowledge, this level of stability surpasses even that reported recently for best-in-class Li-S full batteries.[3a, 3b, 16] Additionally, the charge and discharge voltage profiles of the full cells show a low cell polarization of 153 mV with typical voltage plateaus that correspond to the subsequent redox reactions of polysulfide in a sulfur electrode (**Figure S12a**).[16c] Furthermore, the cell demonstrates a high Coulombic efficiency of nearly 100% and capacity of 1198 mAh g^{-1}, 951 mAh g^{-1}, 723 mAh g^{-1}, 501 mAh g^{-1}, 307 mAh g^{-1}, and 201 mAh g^{-1} at dynamic current density rates of 0.1C, 0.2C, 0.5C, 1C, 2C, and 3C, respectively (**Figure 5h**). For comparison purposes, we also present the results of a control full cell based on the conventional Li-S battery electrolyte, namely 1.0 M LiTFSI + 0.4 M $LiNO_3$ in DOL-DME (**Figure 5f-g** and **Figure S12b**). Evidently, the control cell exhibits a large drop in capacity even after only a few cycles. The latter is attributed firstly, to poor Li^+ desolvation, which in turn causes irreversible Li^+-solvent co-insertion at the graphite anode, and secondly to the polysulfide shuttle effect.[16b]

3. Conclusions

The present study unravels important mechanistic insights into the role of electrolyte additives in promoting Li^+ desolvation and its relations to battery operation and performance. Additives,

such as nitrates, are found to incorporate into the Li^+ solvation shells and change the local environment of Li^+ ions as well as Li^+ coordination, resulting in efficient Li^+ desolvation and improved battery performance. Ensuing batteries show reversible Li^+ (de-)intercalation at the graphite anode with superior performance over 250 cycles (340 mAh g^{-1}, 91.4% of theoretical capacity) while simultaneously suppressing the polysulfide shuttle effect in the sulfur cathode. For the first time, we study the SEI formed on the graphite electrodes using *in-situ* measurements and other complementary techniques, to confirm the key role of Li^+ desolvation process on the graphite electrode. Finally, the study is the first to report the application of the inexpensive $NaNO_3$ additive as a viable replacement to the commonly used $LiNO_3$, without compromising the cell's performance. The tri-fold benefits are combined into safe Li-S full batteries with $NaNO_3$ that exhibits enhanced long-term cycle performance (initial capacity of 1153 mAh g^{-1} at 0.25C) and Coulombic efficiency approaching 100% over 300 cycles. The new insights into the key role of Li^+ desolvation have important implications that extend beyond Li-based batteries.

Supporting Information

Supporting Information is available from the Wiley Online Library or from the author.

Conflicts of Interest

There are no conflicts of interest.

Acknowledgments

This work was supported by the King Abdullah University of Science and Technology (KAUST). L.T. acknowledged computational time at the GRNET HPC facility ARIS through project pr007037-STEM-2. W. W. and V. L. contributed equally to this work.

Received: ((will be filled in by the editorial staff))
Revised: ((will be filled in by the editorial staff))
Published online: ((will be filled in by the editorial staff))

References

[1] a) Q. Pang, X. Liang, C. Y. Kwok, L. F. Nazar, *Nat. Energy* **2016**, 1, 16132; b) J. Lu, L. Li, J. B. Park, Y. K. Sun, F. Wu, K. Amine, *Chem. Rev.* **2014**, 114, 5611; c) X. Gao, Z. P. Jovanov, Y. Chen, L. R. Johnson, P. G. Bruce, *Angew. Chem. Int. Ed.* **2017**, 56, 6539.

[2] a) C. Zhan, T. Wu, J. Lu, K. Amine, *Energy Environ. Sci.* **2018**, 11, 243; b) Y.-K. Sun, S.-T. Myung, B.-C. Park, J. Prakash, I. Belharouak, K. Amine, *Nat. Mater.* **2009**, 8, 320; c) Y. Domi, T. Doi, M. Ochida, T. Yamanaka, T. Abe, Z. Ogumi, *J. Electrochem. Soc.* **2016**, 163, A2849.

[3] a) J. Ming, Z. Cao, W. Wahyudi, M. Li, P. Kumar, Y. Wu, J.-Y. Hwang, M. N. Hedhili, L. Cavallo, Y.-K. Sun, L.-J. Li, *ACS Energy Lett.* **2018**, 3, 335; b) D. Lv, P. Yan, Y. Shao, Q. Li, S. Ferrara, H. Pan, G. L. Graff, B. Polzin, C. Wang, J.-G. Zhang, J. Liu, J. Xiao, *Chem. Commun.* **2015**, 51, 13454; c) M. T. Ong, O. Verners, E. W. Draeger, A. C. T. van Duin, V. Lordi, J. E. Pask, *J. Phys. Chem. B* **2015**, 119, 1535.

[4] J. Ming, M. Li, P. Kumar, A.-Y. Lu, W. Wahyudi, L. J. Li, *ACS Energy Lett.* **2016**, 1, 529.

[5] Z. Peng, S. A. Freunberger, Y. Chen, P. G. Bruce, *Science* **2012**, 337, 563.

[6] a) J. Wang, Y. Yamada, K. Sodeyama, C. H. Chiang, Y. Tateyama, A. Yamada, *Nat. Commun.* **2016**, 7, 12032; b) Y. Yamada, M. Yaegashi, T. Abe, A. Yamada, *Chem. Commun.* **2013**, 49, 11194; c) L. Suo, Y.-S. Hu, H. Li, M. Armand, L. Chen, *Nat. Commun.* **2013**, 4, 1481.

[7] a) Y. Yamada, K. Usui, K. Sodeyama, S. Ko, Y. Tateyama, A. Yamada, *Nat. Energy* **2016**, 1, 16129; b) X. He, B. Yan, X. Zhang, Z. Liu, D. Bresser, J. Wang, R. Wang, X. Cao, Y. Su, H. Jia, C. P. Grey, H. Frielinghaus, D. G. Truhlar, M. Winter, J. Li, E. Paillard, *Nat. Commun.* **2018**, 9, 5320.

[8] Y. Yamada, K. Usui, C. H. Chiang, K. Kikuchi, K. Furukawa, A. Yamada, *ACS Appl. Mater. Interfaces* **2014**, 6, 10892.

[9] Y. Yamada, K. Furukawa, K. Sodeyama, K. Kikuchi, M. Yaegashi, Y. Tateyama, A. Yamada, *J. Am. Chem. Soc.* **2014**, 136, 5039.

[10] E. R. Logan, E. M. Tonita, K. L. Gering, J. Li, X. Ma, L. Y. Beaulieu, J. R. Dahn, *J. Electrochem. Soc.* **2018**, 165, A21.

[11] a) T. Zhang, M. Marinescu, S. Walus, P. Kovacik, G. J. Offer, *J. Electrochem. Soc.* **2018**, 165, A6001; b) D. Guo, F. Ming, H. Su, Y. Wu, W. Wahyudi, M. Li, M. N. Hedhili, G. Sheng, L.-J. Li, H. N. Alshareef, Y. Li, Z. Lai, *Nano Energy* **2019**, 61, 478.

[12] a) J. Zheng, M. H. Engelhard, D. Mei, S. Jiao, B. J. Polzin, J.-G. Zhang, W. Xu, *Nat. Energy* **2017**, 2, 17012; b) F. Wu, J. T. Lee, N. Nitta, H. Kim, O. Borodin, G. Yushin, *Adv. Mater.* **2015**, 27, 101.

[13] a) J. Ming, J. Zhang, L. Zhou, H. Ming, Y. Wu, W. Wahyudi, Z. Cao, L. Cavallo, L. Wang, *Chem. Commun.* **2019**, 55, 5713; b) S. S. Zhang, *J. Power Sources* **2006**, 162, 1379; c) J. Ming, Z. Cao, Y. Wu, W. Wahyudi, W. Wang, X. Guo, L. Cavallo, J.-Y. Hwang, A. Shamim, L.-J. Li, Y.-K. Sun, H. N. Alshareef, *ACS Energy Lett.* **2019**, 4, 2613.

[14] a) W. Li, H. Yao, K. Yan, G. Zheng, Z. Liang, Y.-M. Chiang, Y. Cui, *Nat. Commun.* **2015**, 6, 7436; b) A. Rosenman, R. Elazari, G. Salitra, E. Markevich, D. Aurbach, A. Garsuch, *J. Electrochem. Soc.* **2015**, 162, A470; c) B. D. Adams, E. V. Carino, J. G. Connell, K. S. Han, R. Cao, J. Chen, J. Zheng, Q. Li, K. T. Mueller, W. A. Henderson, J.-G. Zhang, *Nano Energy* **2017**, 40, 607; d) S. Liu, G.-R. Li, X.-P. Gao, *ACS Appl. Mater. Interfaces* **2016**, 8, 7783; e) R. Cao, W. Xu, D. Lv, J. Xiao, J.-G. Zhang, *Adv. Energy Mater.* **2015**, 5, 1402273; f) W. Jia, C. Fan, L. Wang, Q. Wang, M. Zhao, A. Zhou, J. Li, *ACS Appl. Mater. Interfaces* **2016**, 8, 15399.

[15] Z. Lin, Z. Liu, W. Fu, N. J. Dudney, C. Liang, *Adv. Funct. Mater.* **2013**, 23, 1064.

[16] a) J. Sun, J. Liang, J. Liu, W. Shi, N. Sharma, W. Lv, R. Lv, Q.-H. Yang, R. Amal, D.-W. Wang, *Energy Environ. Sci.* **2018**, 11, 2509; b) M. Agostini, B. Scrosati, J. Hassoun, *Adv. Energy Mater.* **2015**, 5, 1500481; c) W. Wahyudi, Z. Cao, P. Kumar, M. Li, Y. Wu, M. N. Hedhili, T. D. Anthopoulos, L. Cavallo, L.-J. Li, J. Ming, *Adv. Funct. Mater.* **2018**, 28, 1802244.

[17] L. Suo, O. Borodin, T. Gao, M. Olguin, J. Ho, X. Fan, C. Luo, C. Wang, K. Xu, *Science* **2015**, 350, 938.

[18] a) J. Zhao, L. Wang, X. He, C. Wan, C. Jiang, *J. Electrochem. Soc.* **2008**, 155, A292; b) S. Zugmann, M. Fleischmann, M. Amereller, R. M. Gschwind, H. D. Wiemhöfer, H. J. Gores, *Electrochim. Acta* **2011**, 56, 3926.

[19] D. M. Seo, P. D. Boyle, R. D. Sommer, J. S. Daubert, O. Borodin, W. A. Henderson, *J. Phys. Chem. B* **2014**, 118, 13601.

[20] V. Mohaček-Grošev, K. Furić, H. Ivanković, *Vibrational Spectroscopy* **2013**, 64, 101.

[21] W. Wang, Z. Cao, G. A. Elia, Y. Wu, W. Wahyudi, E. Abou-Hamad, A.-H. Emwas, L. Cavallo, L.-J. Li, J. Ming, *ACS Energy Lett.* **2018**, 3, 2899.

[22] a) L. Zheng, H. Zhang, P. Cheng, Q. Ma, J. Liu, J. Nie, W. Feng, Z. Zhou, *Electrochim. Acta* **2016**, 196, 169; b) M. Nie, B. L. Lucht, *J. Electrochem. Soc.* **2014**, 161, A1001; c) L. Madec, J. Xia, R. Petibon, K. J. Nelson, J.-P. Sun, I. G. Hill, J. R. Dahn, *J. Phys. Chem. C* **2014**, 118, 29608.

[23] a) J.-I. Yamaki, H. Takatsuji, T. Kawamura, M. Egashira, *Solid State Ionics* **2002**, 148, 241; b) Y. Shigematsu, M. Ue, J.-I. Yamaki, *J. Electrochem. Soc.* **2009**, 156, A176; c) N.-S. Choi, Z. Chen, S. A. Freunberger, X. Ji, Y.-K. Sun, K. Amine, G. Yushin, L. F. Nazar, J. Cho, P. G. Bruce, *Angew. Chem. Int. Ed.* **2012**, 51, 9994.

[24] a) B. Jache, J. O. Binder, T. Abe, P. Adelhelm, *Phys. Chem. Chem. Phys.* **2016**, 18, 14299; b) D. Aurbach, E. Zinigrad, Y. Cohen, H. Teller, *Solid State Ionics* **2002**, 148, 405.

[25] Y. Liu, D. Lin, Y. Li, G. Chen, A. Pei, O. Nix, Y. Li, Y. Cui, *Nat. Commun.* **2018**, 9, 3656.

[26] a) N. Yabuuchi, K. Kubota, M. Dahbi, S. Komaba, *Chem. Rev.* **2014**, 114, 11636; b) H. Zhang, Y. Huang, H. Ming, G. Cao, W. Zhang, J. Ming, R. Chen, *J. Mater. Chem.* **2020**, 8, 1604.

[27] J. Zheng, G. Ji, X. Fan, J. Chen, Q. Li, H. Wang, Y. Yang, K. C. DeMella, S. R. Raghavan, C. Wang, *Adv. Energy Mater.* **2019**, 9, 1803774.

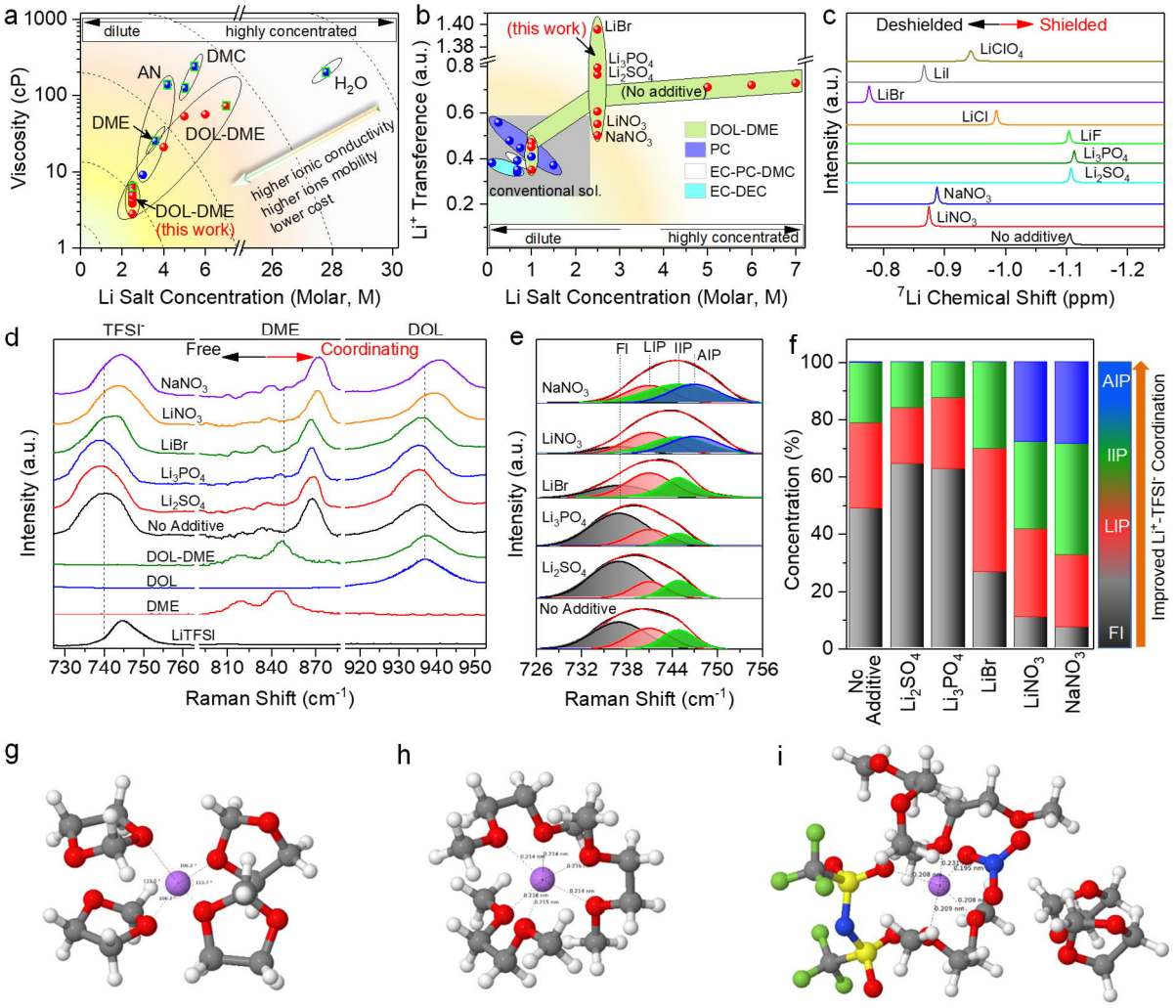

Figure 1. Ion transport behavior: Summary of (a) viscosity and (b) Li^+ transference number (t_{Li+}) of the electrolytes. Green squares in (a) represent improved Li^+ (de-)intercalation or suppressed Li dendrite in the battery. DOL: dioxolane; DME: dimethoxyethane; AN: acetonitrile; DMC: dimethyl carbonate; PC: propylene carbonate; EC: ethylene carbonate; and DEC: diethyl carbonate. **Li^+ desolvation in the electrolytes:** (c) ^{7}Li NMR and (d) Raman spectra of the electrolytes showing S-N stretching in $TFSI^-$ and C-O stretching in DME and DOL. (e) Deconvolution of S-N stretching band in $TFSI^-$ of the electrolytes and (f) concentration ratio of each coordination structure between $TFSI^-$ and Li^+. Structure of Li^+ solvation clusters with (g) 4 DOL and (h) 3 DME molecules, (i) complex of a Li^+, a $TFSI^-$, and a NO_3^- with 3 DME and 2 DOL molecules. (C: gray, H: white, O: red, F: green, S: yellow, N: blue, Li: purple spheres).

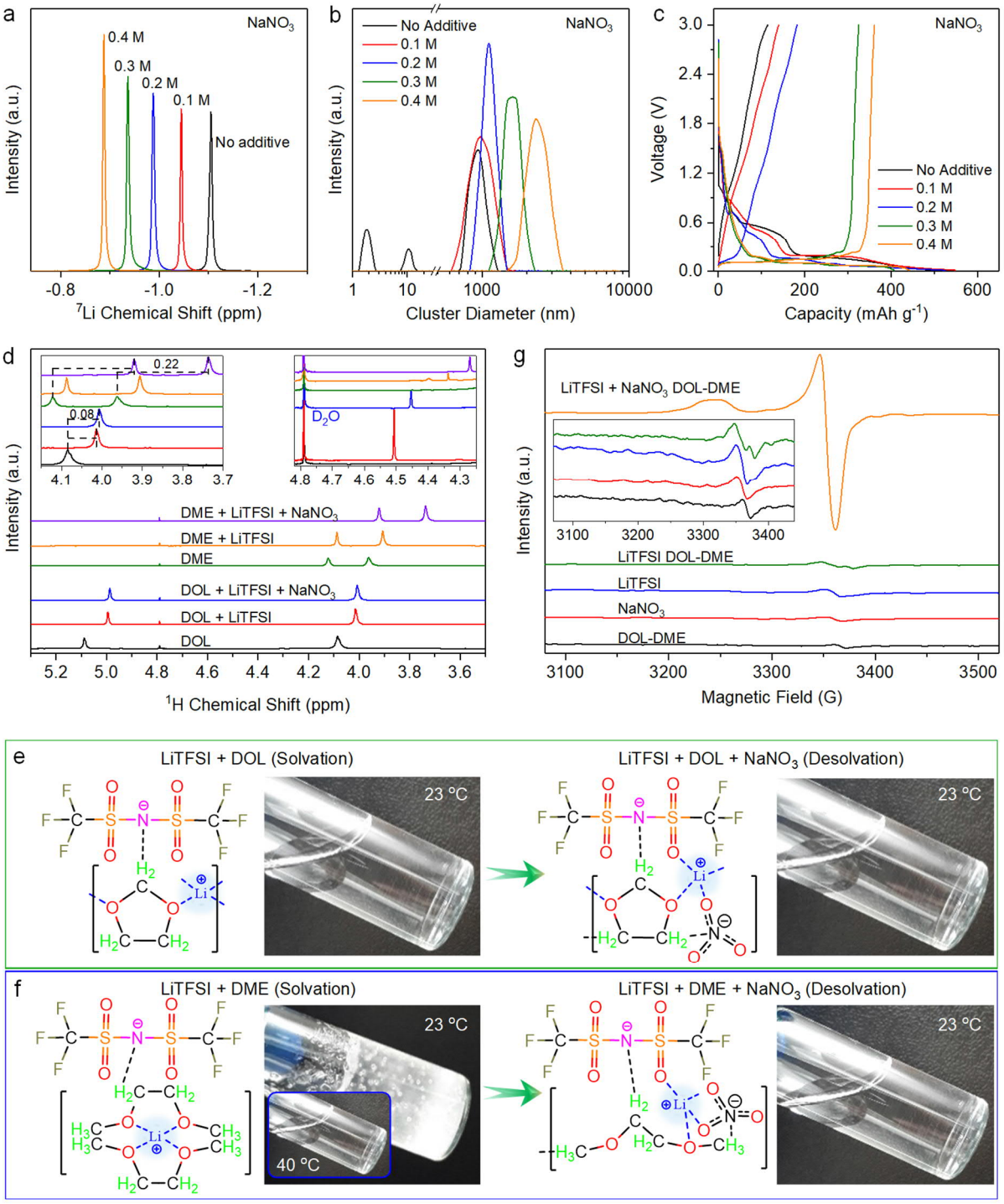

Figure 2. Li^+ desolvation mechanism by nitrate additives: (a) ^7Li NMR and (b) DLS spectra of the electrolytes incorporating $NaNO_3$ additive and (c) their performance in the Li-graphite half-cells. (d) ^1H NMR spectra of electrolytes with a single solvent. Inset: (left) effect of $NaNO_3$ on Li^+ solvation and (right) chemical shift of interaction between $TFSI^-$ and the solvents. Plausible mechanisms of Li^+ desolvation by $NaNO_3$ in the (e) DOL and (f) DME solvents. (g) Electron paramagnetic resonance (EPR) spectra of the electrolyte with $NaNO_3$ additive.

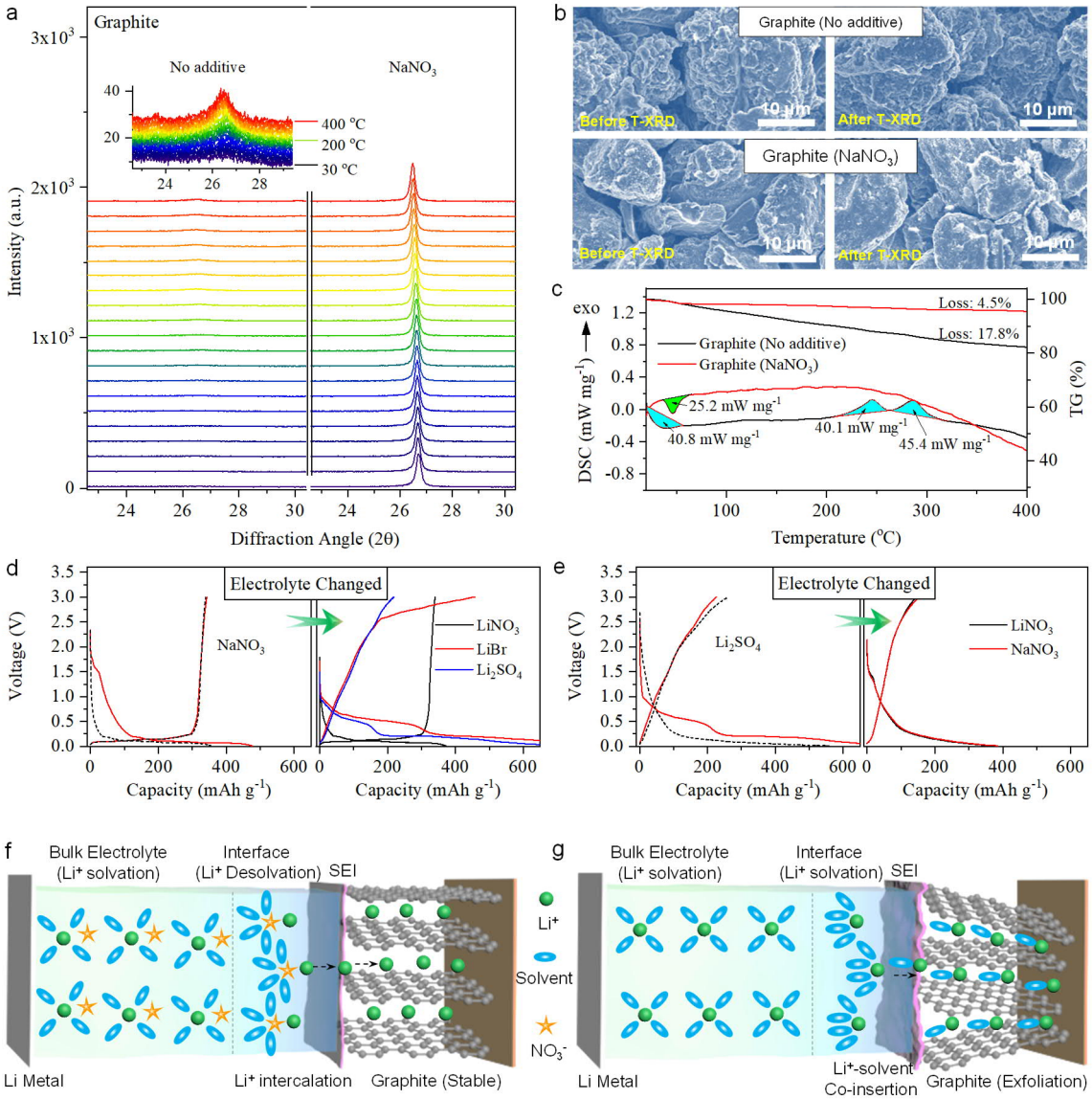

Figure 3. Interfacial study on electrode stability: (a) Temperature-dependent XRD, (b) SEM images, and (c) DSC-TG analysis of cycled graphite with and without $NaNO_3$. (d and e) Charge-discharge profiles of graphite half-cells before and after electrolyte exchange. Schematic of (f) successful Li^+ desolvation leading to Li^+ intercalation and (g) strong Li^+ solvation leading to Li^+-solvent co-insertion at the graphite anode during discharge process.

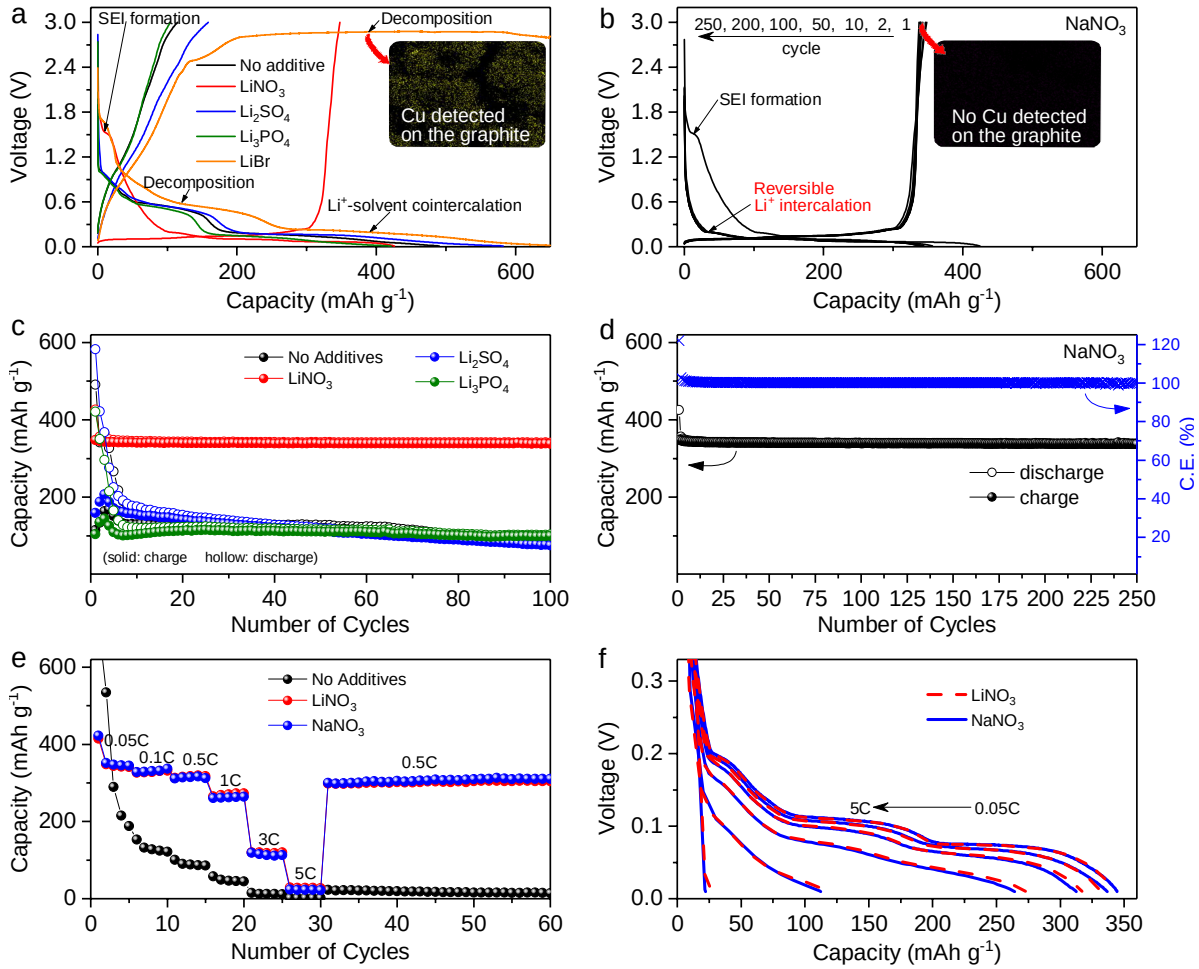

Figure 4. Effects of Li^+ desolvation on Li^+ intercalation: (a) Charge-discharge profiles (first cycle) of graphite half-cells and (b) extended cycles for the electrolyte with $NaNO_3$. Inset: mapping of Cu element on the cycled graphite. (c) Long-term cycle performance of graphite half-cells and (d) extended cycle performance of the cell with $NaNO_3$. (e) Capacity retention and (f) charge-discharge profiles of the cells with nitrate additive from 0.05C to 5C rate.

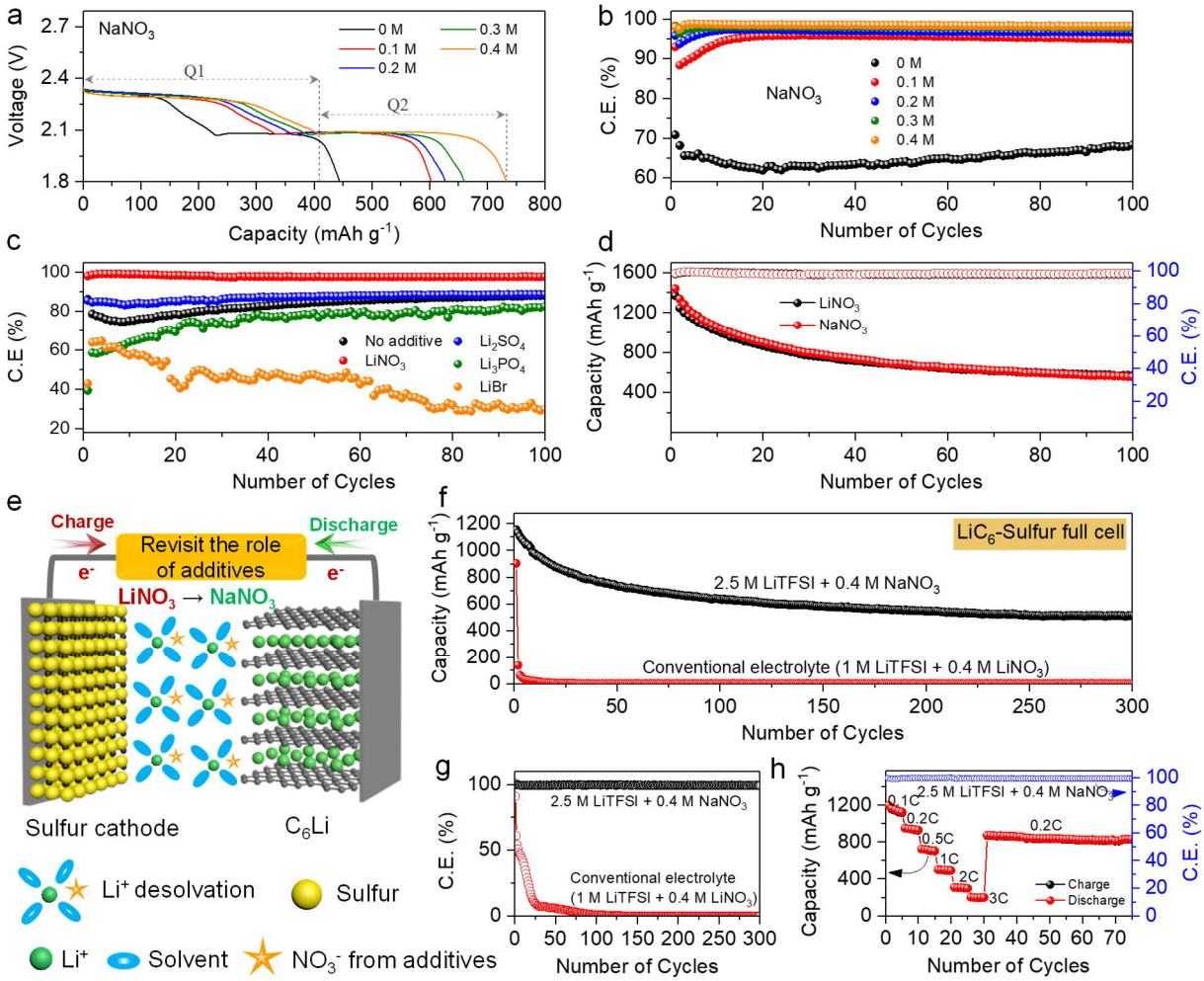

Figure 5. Effects of Li^+ desolvation on polysulfide shuttle effect and safe Li-S full cells: (a) Discharge profiles of the first cycle and (b) Coulombic efficiency of Li-S half-cells at 0.25C with different $NaNO_3$ concentration. (c) Coulombic efficiency of Li-S half-cells with different additives. (d) Identical performance of Li-S half-cells for electrolytes with $LiNO_3$ and $NaNO_3$. (e) Schematic of the Li-S full cell, (f) Long-term cycle performance and (g) Coulombic efficiency of the Li-S full cell in the electrolyte with $NaNO_3$ (black), compared to the conventional Li-S battery electrolyte (red) at 0.25C. (h) Capacity retention of the Li-S full cell from 0.1C to 3C rate.

Table of contents:

The key role of additives in promoting cation (*e.g.*, Li^+) desolvation in the battery electrolytes is unraveled. The nitrate (NO_3^-) anions are found to incorporate into the solvation shells, change the local environment of Li^+ ions as well as the Li^+ coordination in the electrolyte, resulting in effective Li^+ desolvation and enhanced battery performances.

Keywords: electrolyte additives, lithium solvation, graphite anode, lithium batteries, Li-S batteries

W. Wahyudi,† V. Ladelta,† L. Tsetseris, M. M. Alsabban, X. Guo, E. Yengel, H. Faber, B. Adilbekova, A. Seitkhan, A. H. Emwas, M. N. Hedhili, L. J. Li, V. Tung, N. Hadjichristidis, T. D. Anthopoulos,* J. Ming**

Li^+ Desolvation in Ether-based Electrolytes Induced by Nitrate Additives Reveals New Insights into High Performance Lithium Batteries

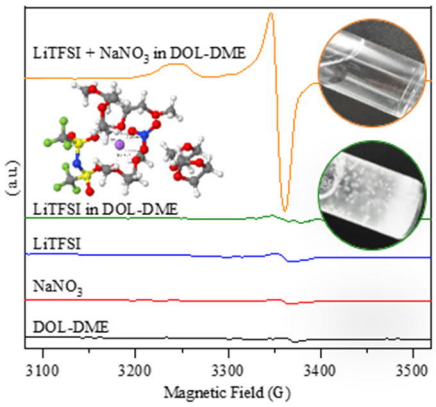

Supporting Information

Li^+ Desolvation in Ether-based Electrolytes Induced by Nitrate Additives Reveals New Insights into High Performance Lithium Batteries

Wandi Wahyudi,[†] Viko Ladelta,[†] Leonidas Tsetseris, Merfat M. Alsabban, Xianrong Guo, Emre Yengel, Hendrik Faber, Begimai Adilbekova, Akmaral Seitkhan, Abdul-Hamid Emwas, Mohammed N. Hedhili, Lain-Jong Li, Vincent Tung, Nikos Hadjichristidis,* Thomas D. Anthopoulos,* Jun Ming*

Experiment

Materials and reagents. Lithium bis(trifluoromethanesulfonyl)imide (LiTFSI) lithium salt, 1,3-dioxolane (DOL), 1,2-dimethoxyethane (DME), $LiNO_3$, $NaNO_3$, Li_2SO_4, Li_3PO_4, LiF, LiCl, LiBr, LiI, $LiClO_4$, graphite, sulfur and all other reagents were purchased from Sigma Aldrich and used as received.

Electrolytes, electrodes, and separators. The electrolyte solutions were prepared by dissolving 2.5 M LiTFSI and 0.4 M additives in a mixture of DOL-DME (volume ratio 1:1). Graphite electrode was prepared using tape cast graphite powder and polyvinylidene fluoride (PVDF) binder (weight ratio 9:1) in N-methyl-2-pyrrolidone (NMP) on a copper foil and then dried at 60 °C in vacuum. The sulfur electrode was prepared by mixing sulfur powder and Super P (weight ratio 7:3), heating at 250 °C for several minutes, and then grinding in a mortar. The sulfur/Super P composite was then mixed with PVDF binder (weight ratio 9:1) in NMP, tape cast on an aluminum foil, and then dried at 40 °C in vacuum. Graphite and sulfur loading in the electrodes were 4.3 mg cm^{-2} and 1.1 - 1.3 mg cm^{-2}, respectively. The separator for half-cells with graphite electrodes was pristine glass fiber (Advantec GC-50), while separators for the sulfur electrode and full cells were glass fiber coated with carbon nanotube paste, as reported elsewhere.[1] In detail, a mixture of CNT paste (Cnano Technology) and PVDF binder (weight ratio 9:1) in NMP was tape cast on glass fiber and then dried at 120 °C prior to use in the battery.

Characterizations. The viscosity of electrolyte solutions was measured with a viscometer (Kyoto Electronics) at room temperature. Li^+ transference number of the electrolytes was measured by the potentiostatic polarization method that combines electrochemical impedance spectroscopy (200 kHz - 10 mHz and 10 mV AC signal) and chronoamperometry polarization (10 mV DC) applied to symmetric cells Li | Li with glass fiber separator (VMP-3 Bio-Logic). The formula to calculate the Li^+ transference number was $t_{Li+} = I_s(\Delta V - R_oI_o) / I_o(\Delta V - R_sI_s)$, where I_o is the initial current when the DC voltage (ΔV) was applied, I_s is the steady-state current, R_o and R_s are resistances before and after DC polarization.[2] The structure of electrolyte

solutions was studied by a confocal Raman spectrometer (Witec alpha 300) with an exciting laser of 532 nm, using quartz cuvettes that tightly sealed with argon atmosphere. Deconvolution of the $TFSI^-$ S-N band was performed by using XPS Peaks software with Shirley type background and previously reported $TFSI^-$ coordination bands of free ions at 737 cm^{-1}, loose ion pairs at 741 cm^{-1}, intimate ion pairs at 745 cm^{-1}, and aggregate ion pairs at 747 cm^{-1}.[3] Nuclear magnetic resonance (NMR) analysis of the electrolytes was performed using a coaxial insert with $LiPF_6$ dissolved in the deteriorated water (D_2O) as the reference (Bruker AV-III 600 MHz Liquid NMR). The electron paramagnetic resonance (EPR) spectra were recorded at room temperature by BrukerBioSpin (Rheinstetten, Germany) with a continuous wave Bruker EMX PLUS spectrometer operating at x-band. Dynamic light scattering (DLS) spectra of the electrolytes were collected by integrating ~180 scans (automatic mode) at room temperature using glass cuvettes (Malvern). Morphology and elemental mapping of the cycled graphite were performed by field emission scanning electron microscope equipped with energy dispersive spectroscopy (FEI Quanta 600). Phase identification of the cycled graphite was examined by powder X-ray diffraction with Cu K-α radiation source at 40 kV and 40 mA (Bruker D8 Advance non-ambient temperature) at various temperatures between 30 - 400 °C with a heating rate of 0.5 °C s^{-1} and a delay time of 3 minutes before measurement at each temperature step in air. Differential scanning calorimetry and thermal gravimetric (DSC-TG) analysis were carried out using Simultaneous Thermal Analyzer (STA, STA 449 F1 Netzsch) in N_2 atmosphere with a heating rate of 5 °C min^{-1}.

Electrochemical analysis. Cycle performance of the cells was carried out by galvanostatic battery cycler (Arbin Instrument and Neware) using 2032-type coin cells. For half-cells with graphite or sulfur electrodes, lithium metal was used as the negative electrode, and the electrolyte was 180 μL. The current densities for the cells with graphite and sulfur electrodes were 0.1C (1C = 372 mA g^{-1}) and 0.25C (1C = 1675 mA g^{-1}), respectively, on the weight basis of active materials. Electrolyte exchange of the graphite half-cells was performed as outlined in

the following. Graphite electrodes were cycled with a lithium metal anode in the first electrolyte. After three cycles the cells were dis-assembled, the graphite electrodes were washed in DOL-DME mixture several times, followed by drying at room temperature in a vacuum oven for three hours and then reused to assemble the new cells with different electrolytes. For Li-S full cells, the cathode was sulfur/Super P composite and the anode was lithiated graphite prepared by the electrochemical method. The cut-off voltage of graphite half-cells, sulfur half-cells, and Li-S full cells was 0.01 - 3.0 V, 1.8 - 3.0 V, and 1.8 - 3.0 V vs Li/Li^+, respectively. All the cells were prepared in an argon-filled glovebox and the electrolytes were stirred prior to using in the cells. The cyclic voltammogram (CV) of electrodes and linear sweep voltammogram (LSV) of current collectors were measured by potentiometer VMP-3 (Bio-Logic). CV analysis was carried out by using three-electrode cells with graphite or sulfur as the working electrode and lithium metal as the reference and counter electrodes at scan rates of 0.05 mV $s^{-1}$and 0.25 mV s^{-1} for graphite and sulfur electrodes, respectively. LSV analysis was carried out at a scan rate of 1.0 mV s^{-1} with copper foil or aluminum foil as the working electrode and lithium metal as the reference and counter electrodes. The graphite half-cells with a lithium metal anode were cycled for 100 cycles (except for the LiBr cell which was only cycled once). Then the cells were dis-assembled and the graphite electrodes were washed in DOL-DME mixture several times, followed by drying under vacuum at room temperature for further characterization. Elemental analysis of SEI on the cycled graphite was performed by X-ray photoelectron spectroscopy (XPS, Kratos) and the obtained spectra were calibrated based on C 1s spectra at 284.4 eV.

Density Functional Theory (DFT) calculation. DFT results on the structural details and relative stability of pertinent molecular complexes were obtained with the quantum chemistry code NWChem,[4] the B3LYP exchange-correlation functional[5] and the DZVP orbital basis.[6] Van der Waals interactions were included with the so-called DFT-D3 method.[7] The results on vibrational frequencies were obtained with the hybrid PBE0 exchange-correlation functional.[8]

Supplementary Text

The cyclic voltammogram (CV) of the graphite electrode (red curves in **Figure S6a**) shows that the reversible Li^+ intercalation at graphite only appears in the electrolytes with nitrate additives as they show both typical anodic and cathodic formation of a graphite intercalated compound.[9] In contrast, the other electrolytes show not only irreversible Li^+ intercalation, but also small oxidative reactions at a potential above 2.4 V, which indicates poor chemical stability of the electrolytes. The linear sweep voltammogram (LSV) of the copper current collector (blue curves in **Figure S6a**) shows a dramatic oxidation of copper in the electrolyte with the LiBr additive beyond 2.4 V. Both CV and LSV analysis confirm that nitrate additives thermodynamically allow for the reversible Li^+ intercalation at the graphite anode as well as suppressed oxidation of the copper current collector in the dilute electrolyte solutions. The oxidation of Cu current collector upon the use of additives is presented here to show the disadvantage of some particular additives in the electrolyte. For instances, apart from LiBr is good for Li^+ desolvation as shown by NMR and Raman analysis (**Figure 1b-d**), but Br^- ion leads to a side effect of oxidation of Cu at potential beyond 2.4 V. The similar disadvantage also appears in the electrolytes with Li_2SO_4, Li_3PO_4, LiCl, LiI, and $LiClO_4$.

CV analysis of the sulfur cathode (red curve in **Figure S6b**) shows both anodic and cathodic peaks that correspond to the subsequent redox reactions of polysulfide in typical sulfur electrodes.[1, 10] Remarkably, the Li-S cells with $LiNO_3$ and $NaNO_3$ show much shorter gaps between the tails of the two peaks (*i.e.*, 95 mV and 100 mV, respectively), which indicates that the polysulfide conversion takes place with faster reaction kinetics so that the polysulfide shuttle effect is successfully suppressed.[11] The fast kinetics of polysulfide conversion in the Li-S cells could be attributed to the high population of Li^+-$TFSI^-$ ion pairs in the electrolytes. In contrast, the Li-S cells with the LiBr and $LiClO_4$ additives suffer from severe shuttle effect along with poor polysulfide conversion as the CV curves show no obvious peaks and gaps during the reduction of polysulfide.[10] In addition, the Li-S cells with Li_2SO_4 and Li_3PO_4 additives show

slower polysulfide conversion kinetics because the Li^+-$TFSI^-$ coordination is hampered, as confirmed by the poor Li^+ desolvation effect (**Figure 1c-d**) and the predominant structure of free $TFSI^-$ in **Figure 1e**. LSV analysis of the aluminum current collector (blue curve in **Figure S6b**) shows that the current collector is stable in all the electrolyte solutions at the given working potential of the sulfur cathode, *i.e.*, 1.8 - 3.0 V.

Table S1. Summary of Li^+ transference number and viscosity obtained from this work and from recently reported electrolyte solutions with and without additives. The chronoamperometry (DC polarization) of the electrolytes was measured with 10 mV DC voltage and the viscosity was measured at room temperature.

Electrolyte Type	Li-Salt (Molar, M)	Additive (Molar, M)	Li Transference (t_{Li})	Viscosity (cP)	Solvent	Salt	Additive
This work	2.5	0	0.68 ± 0.0064	2.80 ± 0.057	DOL-DME	LiTFSI	No additive
	2.5	0.4	0.55 ± 0.0407	6.42 ± 0.070	DOL-DME	LiTFSI	$LiNO_3$
	2.5	0.4	0.50 ± 0.0077	6.04 ± 0.044	DOL-DME	LiTFSI	$NaNO_3$
	2.5	0.4	0.77 ± 0.0715	4.49 ± 0.081	DOL-DME	LiTFSI	Li_2SO_4
	2.5	0.4	0.79 ± 0.0967	3.81 ± 0.025	DOL-DME	LiTFSI	Li_3PO_4
	2.5	0.4	1.40 ± 0.0462	5.32 ± 0.051	DOL-DME	LiTFSI	LiBr
	2.5	0.4	0.65 ± 0.0517	3.96 ± 0.019	DOL-DME	LiTFSI	LiF
	2.5	0.4	0.66 ± 0.0134	4.18 ± 0.022	DOL-DME	LiTFSI	LiCl
	2.5	0.4	0.98 ± 0.0441	5.56 ± 0.052	DOL-DME	LiTFSI	LiI
	2.5	0.4	0.83 ± 0.0053	4.84 ± 0.083	DOL-DME	LiTFSI	$LiClO_4$
Ref.[12]	5.03	-	-	124.2	DMC	LiFSA	-
	5.49	-	-	238.9	DMC	LiFSA	-
Ref.[9a]	3.6	-	-	25.1	DME	LIFSA	-
Ref.[2c]	2	-	0.479	20	DOL-DME	LiTFSI	-
	4	-	0.485	21	DOL-DME	LiTFSI	-
	5	-	0.71	53	DOL-DME	LiTFSI	-
	6	-	0.72	56	DOL-DME	LiTFSI	-
	7	-	0.729	72	DOL-DME	LiTFSI	-
Ref.[13]	27.8		-	203	H_2O	LiTFSI	
Ref.[3b]	3	-	-	9.029	AN	LiFSA	-
	4.2	-	-	138.3	AN	LiFSA	-
Ref.[2d]	1	-	0.47	-	DOL-DME	LiTFSI	-
	1	0.4	0.35	-	DOL-DME	LiTFSI	$LiNO_3$
	1	0.4 0.05	0.45	-	DOL-DME	LiTFSI	$LiNO_3$ Li_2S_8
Ref.[2b]	0.68	-	0.34	-	EC-DEC	LiPF6	-
	0.1	-	0.38	-	EC-DEC	LiDFOB	-
	0.68	-	0.35	-	PC	LiBF4	-
	0.68	-	0.39	-	EC-PC-DMC	LiPF6	-
Ref.[2a]	0.25	-	0.557	-	PC	LiPF6	-
	0.5	-	0.477	-	PC	LiPF6	-
	0.75	-	0.445	-	PC	LiPF6	-
	1	-	0.408	-	PC	LiPF6	-
	1.5	-	0.37	-	PC	LiPF6	-

DOL: dioxolane; DME: dimethoxyethane; AN: acetonitrile; DMC: dimethyl carbonate; PC: propylene carbonate; EC: ethylene carbonate; and DEC: diethyl carbonate.
1 Molar = 1 mol L^{-1} (International Union of Pure and Applied Chemistry, IUPAC)

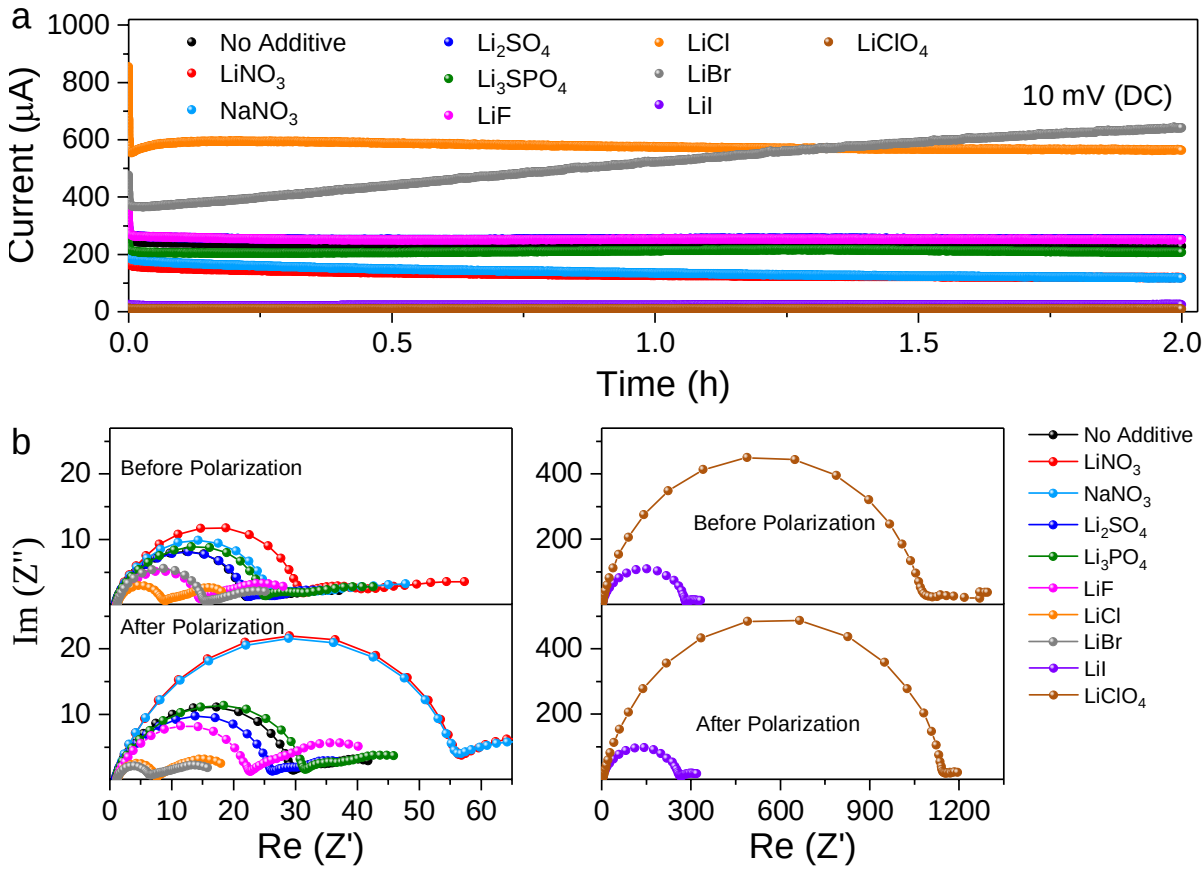

Figure S1. (a) Chronoamperometry polarization of the electrolytes with different additives, measured in Li| Li symmetric cells at 10 mV DC polarization. (b) Electrochemical impedance spectroscopy (EIS) of Li | Li symmetric cells with different electrolyte additives, measured before and after the chronoamperometry polarization, which was used for calculating the Li^+ transference number.

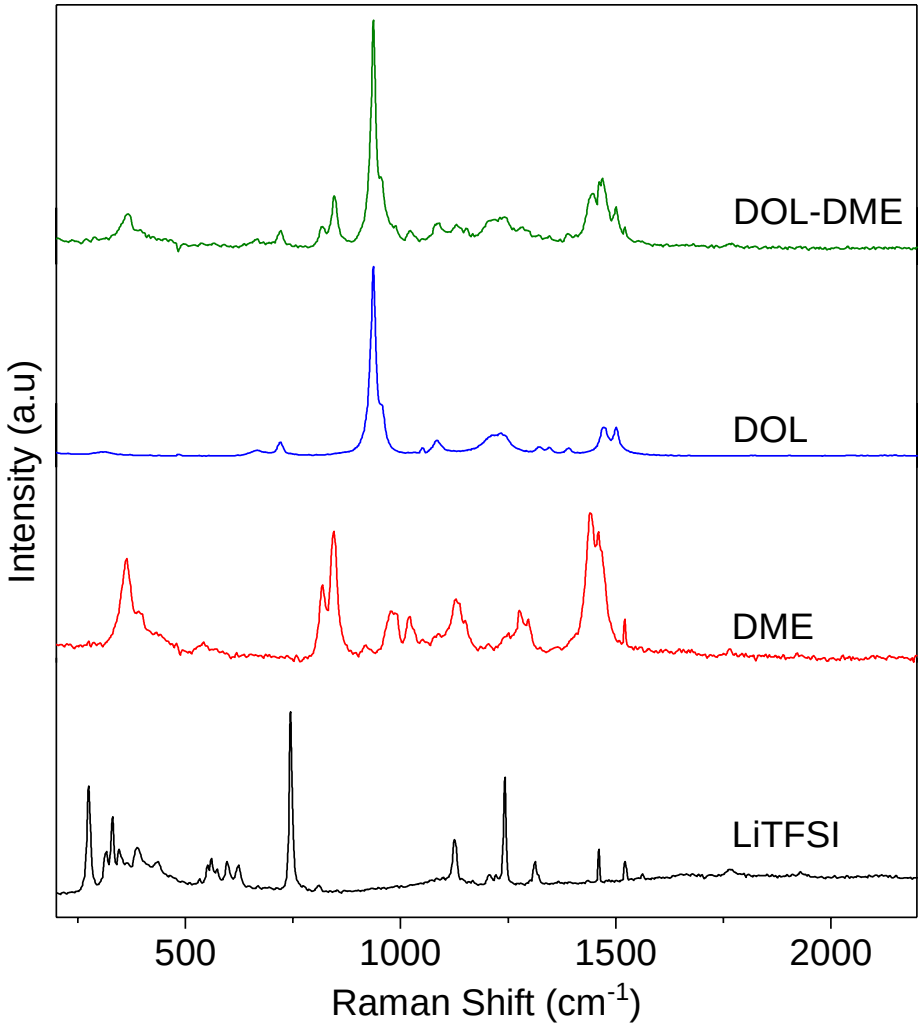

Figure S2. Raman spectra of the LiTFSI salt and solvents (DOL and DME) as the main components in the electrolytes.

5

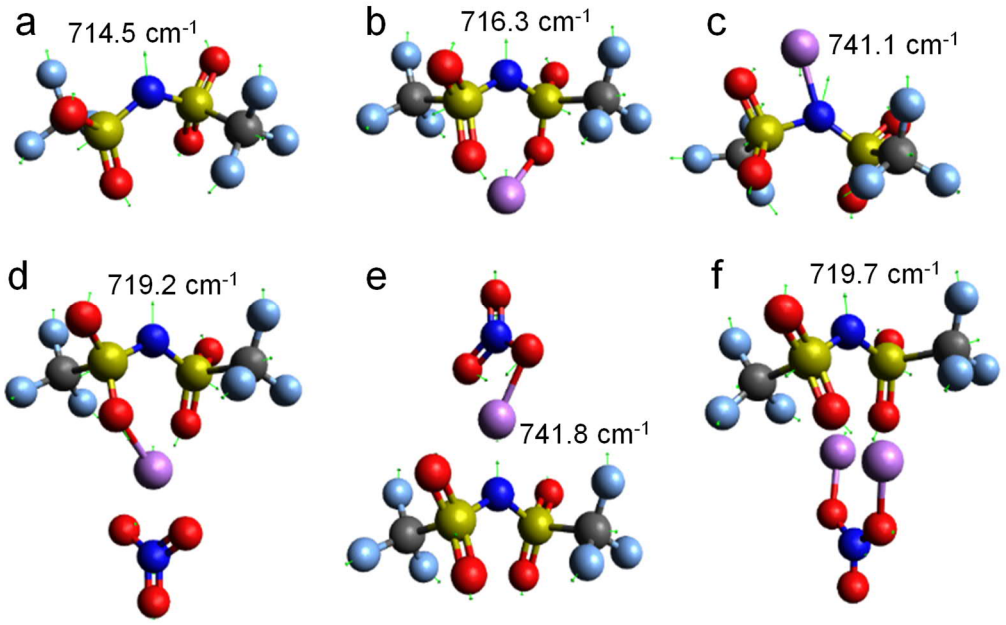

Figure S3. DFT results on the S-N stretching modes (shown with green arrows) of (a) free $TFSI^-$ anion, (b)-(c) LiTFSI free molecules, (c) is less stable than (b) by 0.38 eV, (d)-(e) LiTFSI complex with a NO_3^- anion, (e) is less stable than (d) by 0.20 eV, and (f) LiTFSI complex with a $LiNO_3$ molecule (C: gray, O: red, N: blue, F: light blue, S: yellow, Li: purple spheres).

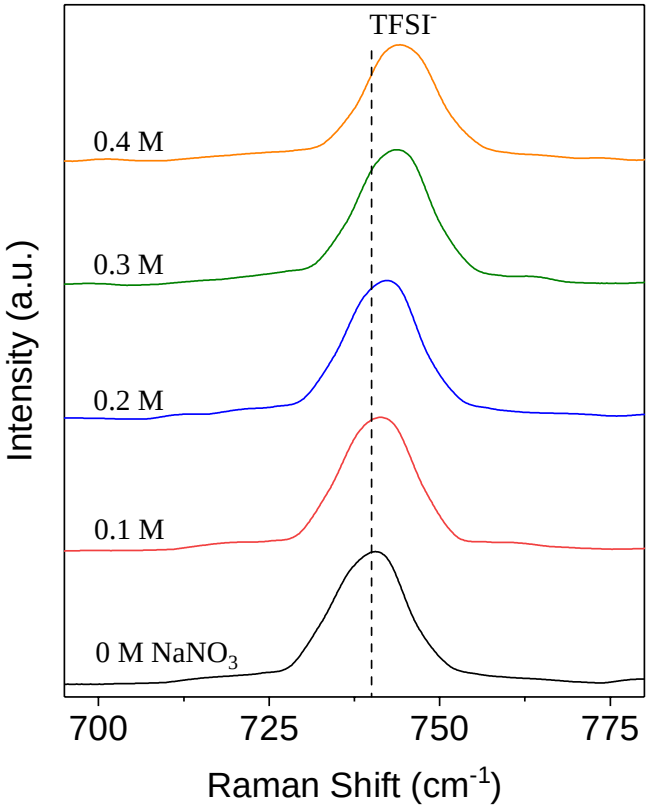

Figure S4. Raman spectra of the electrolytes incorporating $NaNO_3$ additive at different concentrations showing a gradual shift of S-N stretching band in the $TFSI^-$ anions.

5

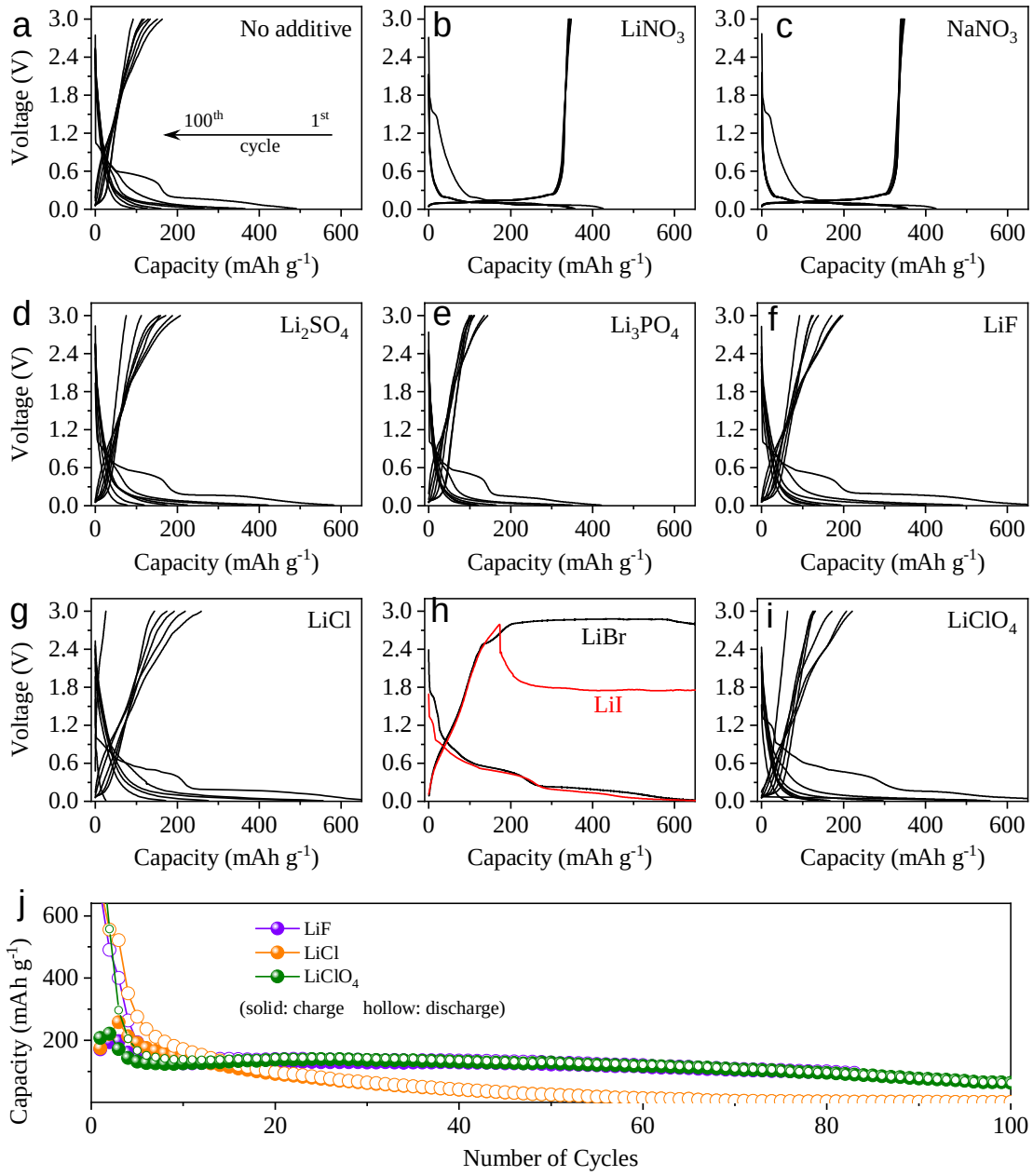

Figure S5. Charge-discharge voltage profiles of long-term cycle of graphite half-cells for the electrolytes with different additives: (a) pristine electrolyte, (b-c) nitrates ($LiNO_3$ and $NaNO_3$), (d) Li_2SO_4, (e) Li_3PO_4, and (f) LiF, (g) LiCl, (h) LiBr and LiI, and (i) $LiClO_4$. (j) Long-term cycle performance of graphite half-cells in the electrolytes with LiF, LiCl, and $LiClO_4$ additives.

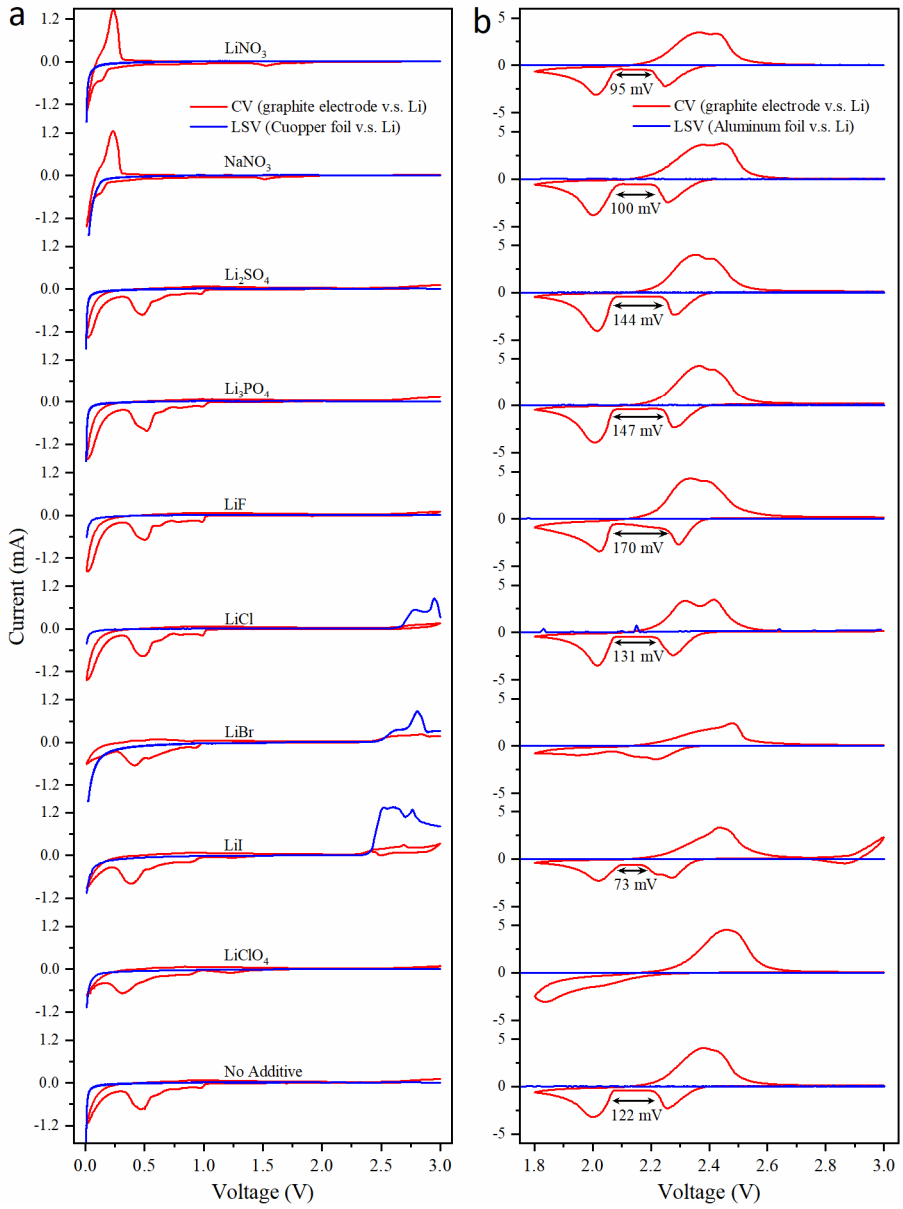

Figure S6. Linear sweep voltammetry (blue curve) of (a) copper and (b) aluminum current collectors in the electrolytes measured at scan rate 1.0 mVs^{-1}. Cyclic voltammetry (red curve) of (a) graphite at scan rate 0.05 mV s^{-1} and (b) sulfur electrodes at scan rate 0.25 mV s^{-1} in the half-cells using different electrolyte additives.

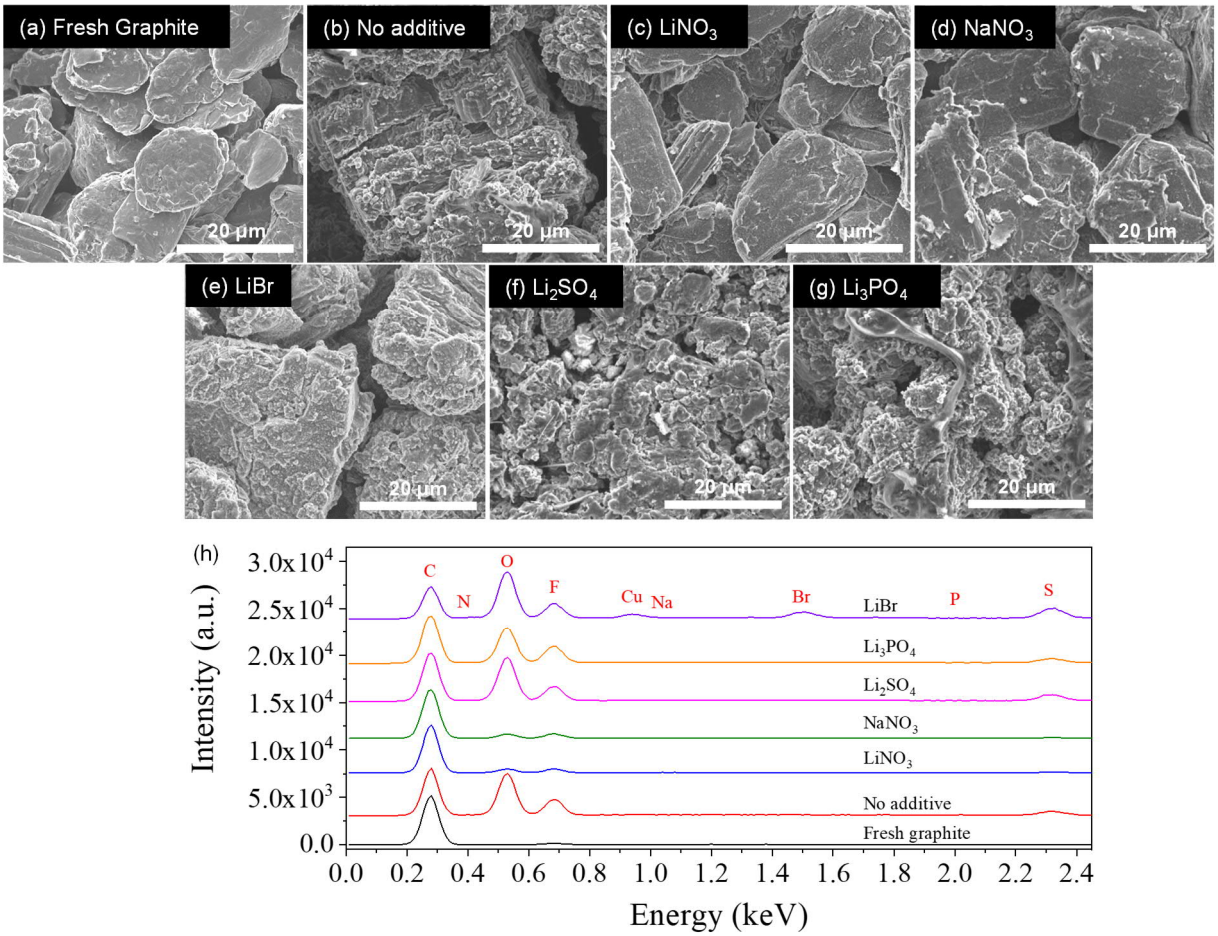

Figure S7. Scanning electron microscope (SEM) images of graphite electrodes after long-term charge-discharge cycles: (a) the fresh graphite electrode was analyzed after drying in a vacuum oven; graphite electrode in the electrolytes with (b) no additive, (c) $LiNO_3$, (d) $NaNO_3$, (e) LiBr, (f) Li_2SO_4, and (g) Li_3PO_4 were cycled for 100 cycles. (h) Electron dispersive spectroscopy (EDS) of graphite electrodes after 100 cycles. Graphite in the electrolyte with LiBr additive was cycled only once as it would not cycle any further. Scale bar: 20 µm.

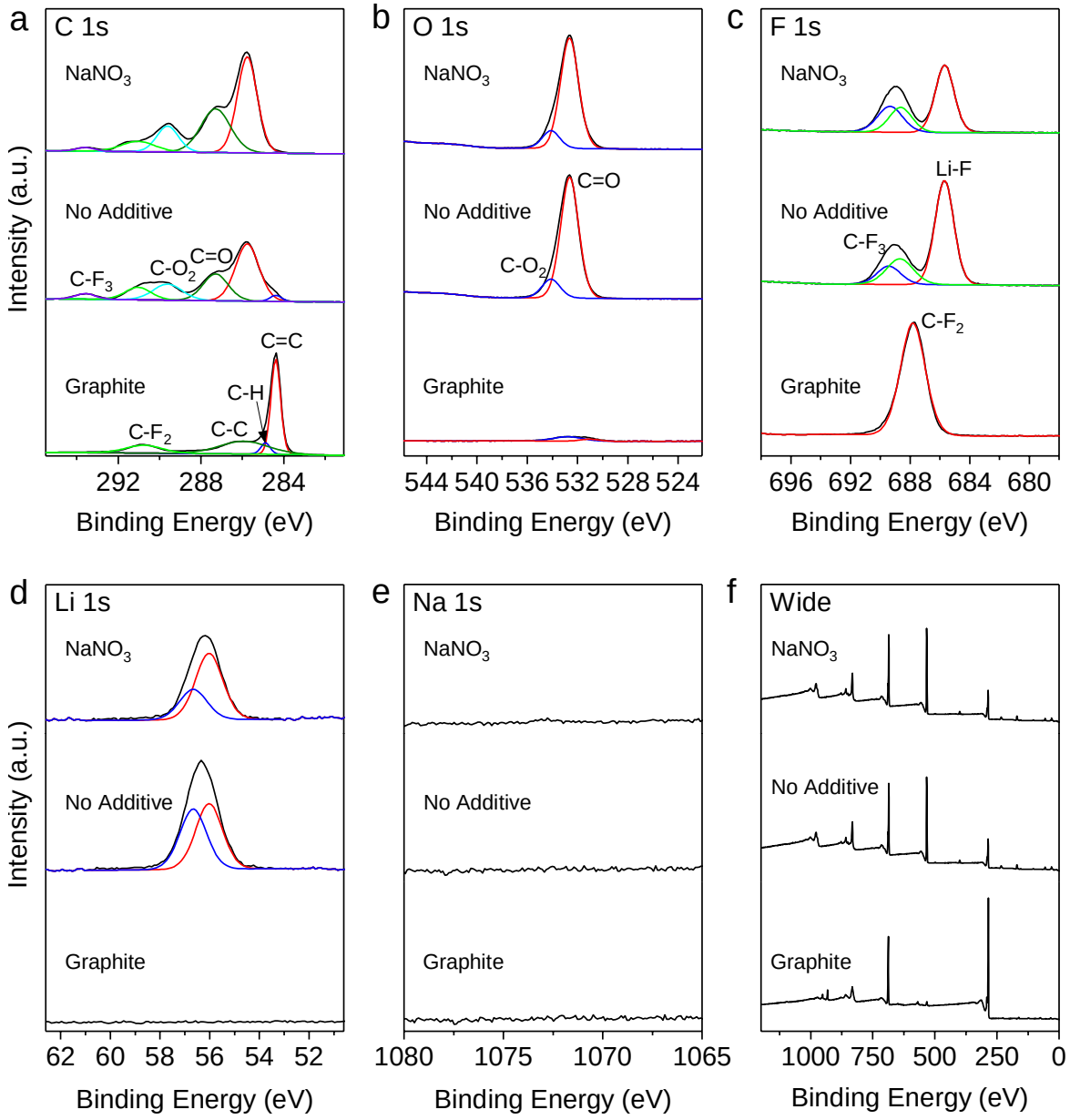

Figure S8. X-ray photoelectron spectroscopy (XPS) analysis on the surface of graphite electrodes after cycling in the electrolytes with no additive and $NaNO_3$: (a) C 1s, (b) O 1s, (c) F 1s, (d) Li 1s, (e) Na 1s and (f) wide spectra.

Table S2. Elemental ratios of the SEI on the cycled graphite electrodes, measured by XPS surface analysis.

	Element Ratio (%)		
	Graphite	**No Additive**	**$NaNO_3$**
C 1s	80.49	30.62	43.34
N 1s	0.00	1.72	2.06
O 1s	1.76	28.31	23.48
F 1s	17.75	24.77	16.29
S 2p	0.00	1.97	1.13
Li 1s	0.00	12.61	13.67
Na 1s	0.00	0.00	0.03

Table S3. Reversibility of Li^+ intercalation in the graphite half-cells with electrolyte exchange.

Cell	Initial Electrolyte	Initial Performance	Second Electrolyte	Second Performance	Note
1	$NaNO_3$	Reversible	$LiNO_3$	Reversible	No SEI formation observed in the second cell
2	$NaNO_3$	Reversible	LiBr	Not reversible	
3	$NaNO_3$	Reversible	Li_2SO_4	Not reversible	
4	$LiNO_3$	Reversible	$NaNO_3$	Reversible	No SEI formation observed in the second cell
5	$LiNO_3$	Reversible	LiBr	Not reversible	
6	$LiNO_3$	Reversible	Li_2SO_4	Not reversible	
7	Li_2SO_4	Not reversible	$LiNO_3$	Not reversible	SEI formation observed in the second cell
8	Li_2SO_4	Not reversible	$NaNO_3$	Not reversible	SEI formation observed in the second cell
9	LiBr	Not reversible	$LiNO_3$	Not reversible	SEI formation observed in the second cell
10	LiBr	Not reversible	$NaNO_3$	Not reversible	SEI formation observed in the second cell

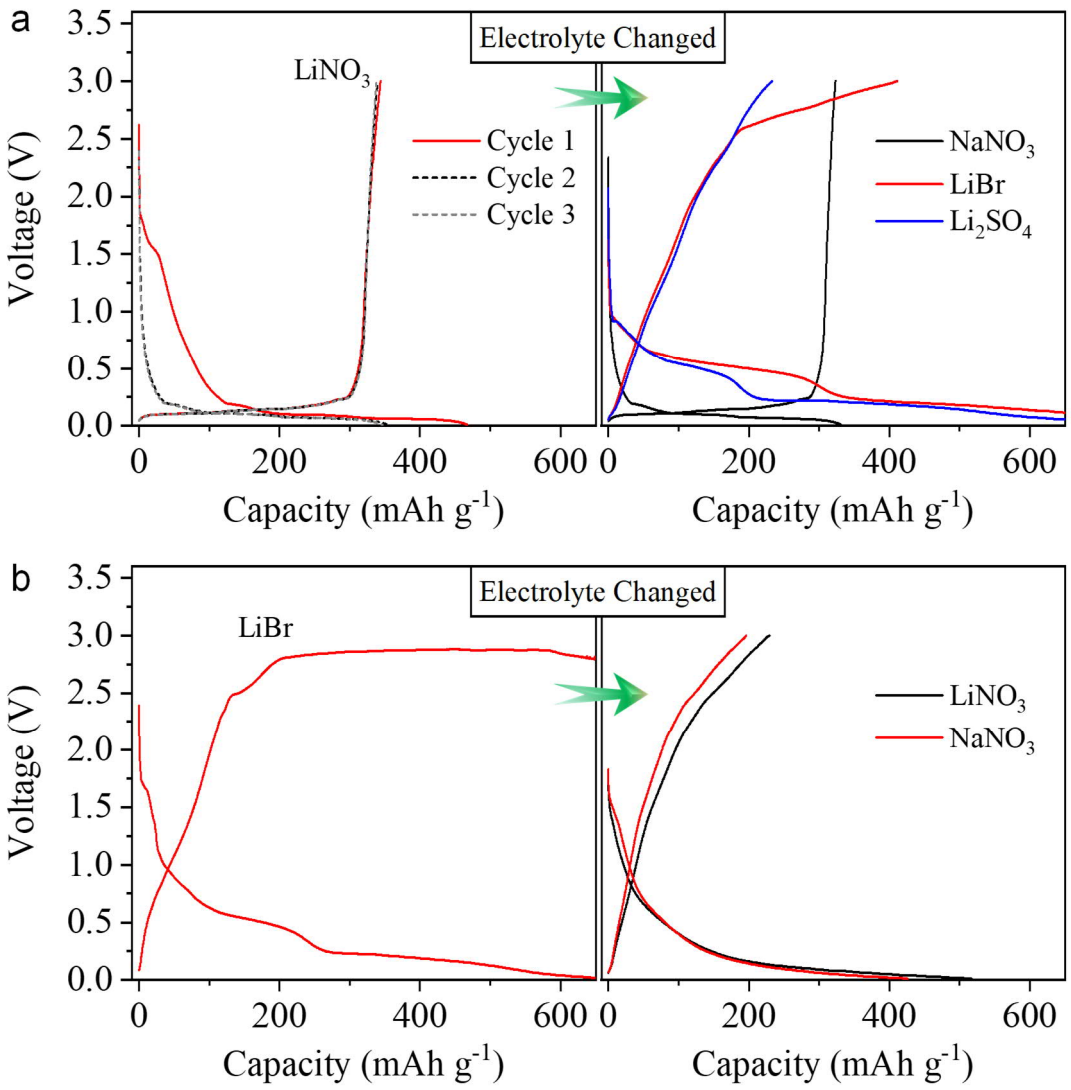

Figure S9. Charge-discharge voltage profiles of graphite half-cells with electrolyte exchange. Firstly, (left) the cells were cycled in the electrolytes with (a) $LiNO_3$ and (b) LiBr additives, and then the cells were dis-assembled and the graphite electrodes were washed, dried, and reused in new cells (right) with different additives for further cycles.

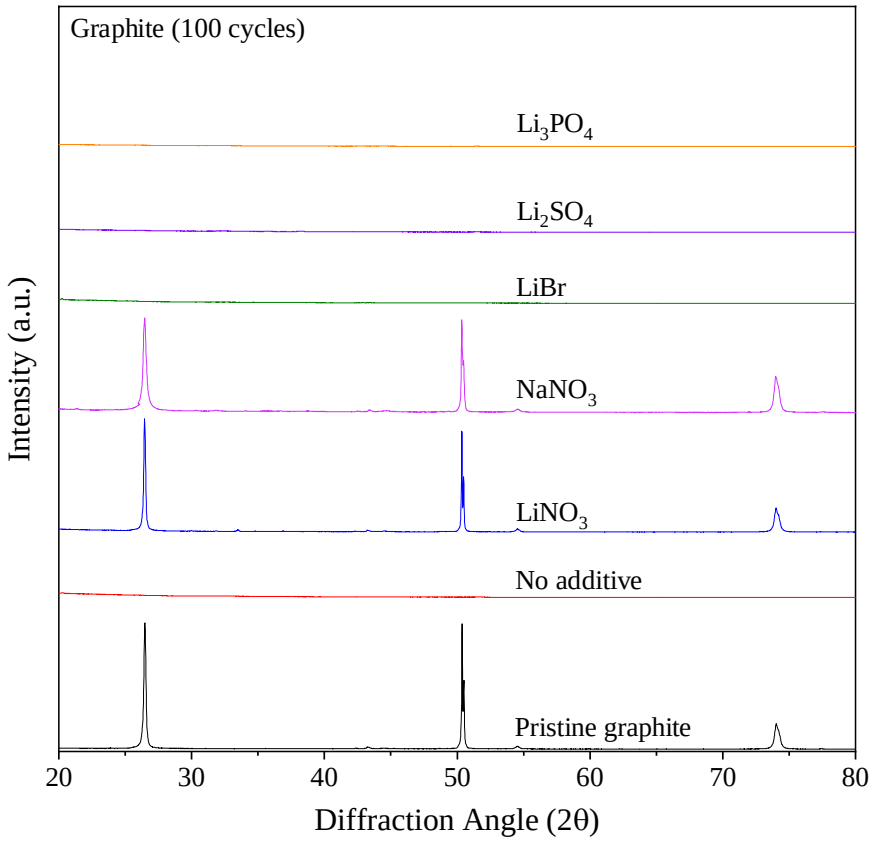

Figure S10. (a) X-ray diffraction (XRD) patterns of graphite electrodes after charge-discharge cycles. The fresh graphite electrode was analyzed after drying in the vacuum oven. The graphite electrode in LiBr electrolyte was cycled only once, and the other graphite electrodes in other electrolytes were cycled for 100 cycles.

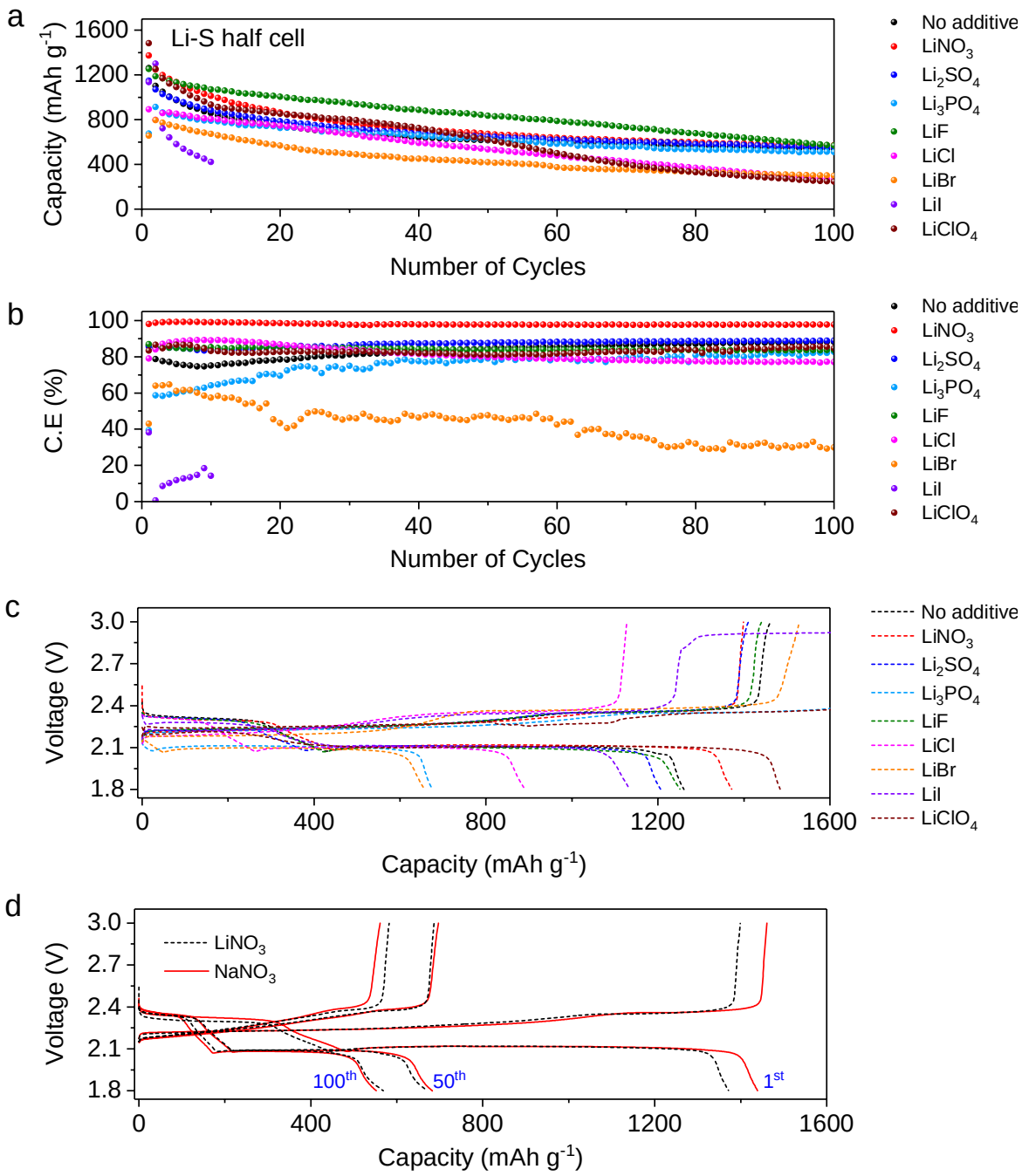

Figure S11. (a) Electrochemical performance and (b) Coulombic efficiency of Li-S half-cells at 0.25C with LiF, LiCl, LiI, and $LiClO_4$ additives. (a) Charge-discharge voltage profiles of Li-S half-cells with different additives. (b) Charge-discharge voltage profiles of long-term cycles of the Li-S half-cells with $LiNO_3$ and $NaNO_3$ additives.

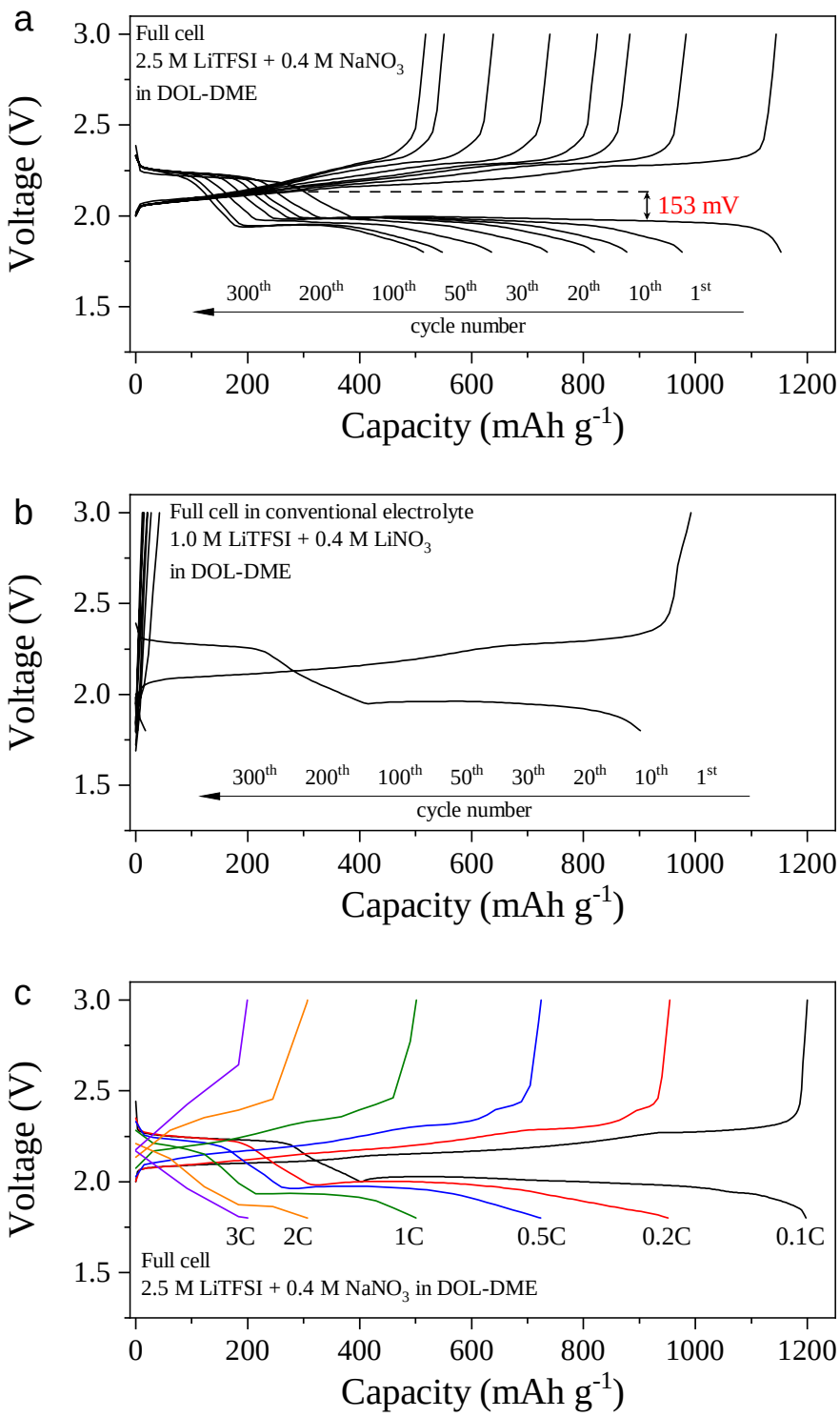

Figure S12. Charge-discharge voltage profiles of Li-S full cells in (a) 2.5 M LiTFSI + 0.4 M $NaNO_3$ in DOL-DME and (b) conventional electrolyte of 1.0 M LiTFSI + 0.4 M $LiNO_3$ at 0.25C. (c) Charge-discharge voltage profiles of the full cell with 2.5 M LiTFSI + 0.4 M $NaNO_3$ in DOL-DME electrolyte at dynamic current density rate from 0.1C to 3C.

SI References

[1] W. Wahyudi, Z. Cao, P. Kumar, M. Li, Y. Wu, M. N. Hedhili, T. D. Anthopoulos, L. Cavallo, L.-J. Li, J. Ming, *Adv. Funct. Mater.* **2018**, 28, 1802244.

[2] a) J. Zhao, L. Wang, X. He, C. Wan, C. Jiang, *J. Electrochem. Soc.* **2008**, 155, A292; b) S. Zugmann, M. Fleischmann, M. Amereller, R. M. Gschwind, H. D. Wiemhöfer, H. J. Gores, *Electrochim. Acta* **2011**, 56, 3926; c) L. Suo, Y.-S. Hu, H. Li, M. Armand, L. Chen, *Nat. Commun.* **2013**, 4, 1481; d) M. Agostini, B. Scrosati, J. Hassoun, *Adv. Energy Mater.* **2015**, 5, 1500481.

[3] a) J. Ming, Z. Cao, W. Wahyudi, M. Li, P. Kumar, Y. Wu, J.-Y. Hwang, M. N. Hedhili, L. Cavallo, Y.-K. Sun, L.-J. Li, *ACS Energy Lett.* **2018**, 3, 335; b) Y. Yamada, K. Furukawa, K. Sodeyama, K. Kikuchi, M. Yaegashi, Y. Tateyama, A. Yamada, *J. Am. Chem. Soc.* **2014**, 136, 5039.

[4] M. Valiev, E. J. Bylaska, N. Govind, K. Kowalski, T. P. Straatsma, H. J. J. Van Dam, D. Wang, J. Nieplocha, E. Apra, T. L. Windus, W. A. de Jong, *Comput. Phys. Commun.* **2010**, 181, 1477.

[5] a) A. D. Becke, *J. Chem. Phys.* **1993**, 98, 5648; b) P. J. Stephens, F. J. Devlin, C. F. Chabalowski, M. J. Frisch, *J. Phys. Chem.* **1994**, 98, 11623.

[6] N. Godbout, D. R. Salahub, J. Andzelm, E. Wimmer, *Can. J. Chem.* **1992**, 70, 560.

[7] S. Grimme, J. Antony, S. Ehrlich, H. Krieg, *J. Chem. Phys.* **2010**, 132, 154104.

[8] J. P. Perdew, M. Ernzerhof, K. Burke, *J. Chem. Phys.* **1996**, 105, 9982.

[9] a) Y. Yamada, M. Yaegashi, T. Abe, A. Yamada, *Chem. Commun.* **2013**, 49, 11194; b) Y. Yamada, K. Usui, C. H. Chiang, K. Kikuchi, K. Furukawa, A. Yamada, *ACS Appl. Mater. Interfaces* **2014**, 6, 10892; c) H. Tavassol, E. M. C. Jones, N. R. Sottos, A. A. Gewirth, *Nat. Mater.* **2016**, 15, 1182.

[10] M. Li, W. Wahyudi, P. Kumar, F. Wu, X. Yang, H. Li, L.-J. Li, J. Ming, *ACS Appl. Mater. Interfaces* **2017**, 9, 8047.

[11] J. Ming, M. Li, P. Kumar, A.-Y. Lu, W. Wahyudi, L.-J. Li, *ACS Energy Lett.* **2016**, 1, 529.

[12] J. Wang, Y. Yamada, K. Sodeyama, C. H. Chiang, Y. Tateyama, A. Yamada, *Nat. Commun.* **2016**, 7, 12032.

[13] Y. Yamada, K. Usui, K. Sodeyama, S. Ko, Y. Tateyama, A. Yamada, *Nat. Energy* **2016**, 1, 16129.